

1 Simulating Lagrangian Subgrid-Scale Dispersion on 2 Neutral Surfaces in the Ocean

3 Daan Reijnders¹, Eric Deleersnijder², Erik van Sebille¹

4 ¹Institute for Marine and Atmospheric research Utrecht, Utrecht University, Utrecht, the Netherlands

5 ²Université catholique de Louvain, Institute of Mechanics, Materials and Civil Engineering (IMMC) &
6 Earth and Life Institute (ELI), Louvain-la-Neuve, Belgium

7 **Key Points:**

- 8 • We create a 3D isoneutral version of the Markov-1 Lagrangian dispersion model,
9 similar to Redi's isopycnal rotation of the diffusion tensor.
- 10 • Dispersion from Markov-1 includes ballistic and diffusive regimes, making trajec-
11 tories more realistic than those from random walk models.
- 12 • Markov-1 produces a much smaller spurious diapycnal diffusivity than Markov-
13 0 (random walk).

Corresponding author: Daan Reijnders, b.j.h.r.reijnders@uu.nl

Abstract

To capture the effects of mesoscale turbulent eddies, coarse-resolution Eulerian ocean models resort to tracer diffusion parameterizations. Likewise, the effect of eddy dispersion needs to be parameterized when computing Lagrangian pathways using coarse flow fields. Dispersion in Lagrangian simulations is traditionally parameterized by random walks, equivalent to diffusion in Eulerian models. Beyond random walks, there is a hierarchy of stochastic parameterizations, where stochastic perturbations are added to Lagrangian particle velocities, accelerations, or hyper-accelerations. These parameterizations are referred to as the 1st, 2nd and 3rd order ‘Markov models’ (Markov-N), respectively. Most previous studies investigate these parameterizations in two-dimensional setups, often restricted to the ocean surface. On the other hand, the few studies that investigated Lagrangian dispersion parameterizations in three dimensions, where dispersion is largely restricted to neutrally buoyant surfaces, have focused only on random walk (Markov-0) dispersion. Here, we present a three-dimensional isoneutral formulation of the Markov-1 model. We also implement an anisotropic, shear-dependent formulation of random walk dispersion, originally formulated as a Eulerian diffusion parameterization. Random walk dispersion and Markov-1 are compared using an idealized setup as well as more realistic coarse and coarsened (50 km) ocean model output. While random walk dispersion and Markov-1 produce similar particle distributions over time when using our ocean model output, Markov-1 yields Lagrangian trajectories that better resemble trajectories from eddy-resolving simulations. Markov-1 also yields a smaller spurious diapycnal flux.

Plain Language Summary

Turbulent eddies stir and disperse material in the ocean. Depending on the resolution of ocean models, these eddies can have length scales that are too small to be resolved explicitly, so they need to be represented by parameterizations. This implies that when particle pathways are computed in Lagrangian simulations, the effect of eddy dispersion also needs to be parameterized. This is traditionally done by adding a random walk on top of successive particle positions. An improvement of this parameterization, referred to as the Markov-1 model, adds random perturbations to particle velocities instead. Dispersion parameterizations have been studied primarily at the surface in two dimensions. In contrast, eddies in the ocean interior predominantly stir and disperse along tilted surfaces of neutral buoyancy. We present a novel three-dimensional formulation of the Markov-1 model and compare it to the random walk model in an idealized setup, as well as using more realistic coarse and coarsened (50 km) ocean model output. Particle distributions produced by both models are similar, but the trajectories produced by Markov-1 better resemble trajectories from simulations that explicitly resolve eddies. Markov-1 also is better able to restrict particle movement to the tilted neutral buoyancy surfaces.

1 Introduction

Turbulent stirring in the ocean disperses tracers and suspended material over time. The eddies, jets, and fronts that characterize this turbulent motion occur at a range of spatial and temporal scales. Since ocean models have a finite resolution, structures with spatial scales of the order of the grid resolution or smaller are not resolved explicitly. Current state-of-the-art global ocean models use nominal $1/48^\circ$ grid resolutions (Su et al., 2018; Fox-Kemper et al., 2019), resolving the mesoscale and part of the mesoscale spectrum. Still, computational constraints limit the simulation length of models at such resolutions to only a few years. Many of the latest generation of Earth system models that are used for CMIP6 use ocean grid resolutions of 1° and $1/4^\circ$ (Hewitt et al., 2020). The models at 1° do not resolve any mesoscale eddies. While the $1/4^\circ$ models are eddy-permitting

64 in parts of the ocean, much higher resolutions are required to resolve the first baroclinic
 65 Rossby radius at higher latitudes, such as in the Southern Ocean, where it is $\mathcal{O}(10\text{ km})$
 66 (Chelton et al., 1998). Parameterizations of mesoscale eddies therefore remain vital to
 67 ocean modeling.

68 The spreading of tracers due to unresolved eddies is typically parameterized as a
 69 diffusive processes, with the evolution of a tracer concentration C governed by the advection-
 70 diffusion equation:

$$\frac{\partial C}{\partial t} + \bar{\mathbf{u}} \cdot \nabla C = \nabla \cdot (\mathbf{K} \cdot \nabla C), \quad (1)$$

71 where $\bar{\mathbf{u}}$ is the resolved, large-scale velocity, and \mathbf{K} is the diffusivity tensor. This practice
 72 traces back to Boussinesq’s concept of eddy viscosity (Boussinesq, 1877) and G.I.
 73 Taylor’s work on diffusion (Taylor, 1922), and is still ubiquitous in ocean modeling (Fox-
 74 Kemper et al., 2019). Much research has focused on determining and formulating \mathbf{K} in
 75 order to best represent ocean eddies. This includes aspects like the isopycnal or isoneu-
 76 tral orientation of eddies in the ocean interior (Redi, 1982), their advective effect (Gent
 77 & McWilliams, 1990; Griffies, 1998; Haigh et al., 2021), their diffusivity strength (Abernathey
 78 et al., 2013; Griesel et al., 2014; Wolfram et al., 2015; Nummelin et al., 2020), and their
 79 anisotropy (Le Sommer et al., 2011; Bachman et al., 2020).

80 Spreading of tracers and suspended material can also be investigated through the
 81 Lagrangian framework. Through Lagrangian particle simulations, we can study the path-
 82 ways of fluid parcels and suspended material forward and backward in time (van Sebille
 83 et al., 2018). The Lagrangian framework is an especially useful alternative for the Eu-
 84 lerian framework in studying tracer transport when dealing with point sources (Spivakovskaya
 85 et al., 2007; Wagner et al., 2019). Lagrangian simulations use Eulerian ocean model fields
 86 to advect virtual particles. This means that Lagrangian simulations also require param-
 87 eterizations to represent missing dispersion due to the unresolved scales in the Eulerian
 88 input data.

89 The simplest Lagrangian sub-grid scale dispersion model consists of adding a ran-
 90 dom walk onto a particle’s successive locations. It can be shown that this method is con-
 91 sistent with the advection-diffusion equation (1) (Heemink, 1990; Visser, 1997; Spagnol
 92 et al., 2002), hence it is often referred to as ‘diffusion’ in Lagrangian literature. It is the
 93 simplest member of a hierarchy of stochastic parameterizations that is Markovian in na-
 94 ture, and we will refer to it here as *Markov-0* (Berloff & McWilliams, 2002). ‘Markovian’
 95 relates to the Markov property that each successive displacement in the random walk
 96 is independent from the previous.

97 One shortcoming of Markov-0 is that it, just like the eddy diffusion approximation
 98 in Eulerian models, assumes that eddies have infinitely short time scales. Put differently,
 99 it assumes that there is no autocorrelation in the turbulent velocity of the Lagrangian
 100 particles. This assumption does not hold true for mesoscale eddies, which transport La-
 101 grangian particles coherently (Haller & Yuan, 2000; Berloff & McWilliams, 2002). Eddy
 102 coherence leaves an imprint on the Lagrangian velocity autocorrelation, which can be
 103 separated into an exponentially decaying part and an oscillatory part that is the result
 104 of phase differences between the eddies and background flow (Veneziani et al., 2004; Klocker,
 105 Ferrari, & LaCasce, 2012). Due to this imprint, Markov-0 is only accurate at time scales
 106 when the autocorrelation has decayed away, meaning $t \gg T_L$. Here, T_L is the Lagrangian
 107 timescale, equal to the e -folding timescale of the exponential decay of the autocorrela-
 108 tion (LaCasce, 2008). T_L may vary between timescales of a day (Koszalka et al., 2013)
 109 to several weeks (see section 4.2), depending on the characteristics of the ocean domain
 110 at hand. If one is concerned with timescales equal to or smaller than T_L , Markov-0 is
 111 inadequate for parameterizing subgrid-scale dispersion. Regardless, this is often the only

112 scheme for parameterizing subgrid-scale dispersion implemented in community Lagrangian
113 modeling frameworks (van Sebille et al., 2018).

114 Parameterizations higher in the hierarchy of stochastic models add Markovian noise
115 not on particle locations, but on their velocities (Markov-1), accelerations (Markov-2),
116 or even hyper-accelerations (Markov-3) (Sawford, 1991; Rodean, 1996; Griffa, 1996; Berloff
117 & McWilliams, 2002). In doing so, these models are capable of better representing disper-
118 sion at shorter timescales (for which $t \not\gg T_L$), and they can be informed by statisti-
119 cal variances in velocity, acceleration, and hyper-acceleration, respectively, as well as
120 the timescales over which the autocorrelations of these quantities decay. Further improve-
121 ments have been formulated that include the looping of particles due to eddy coherence
122 (Reynolds, 2002; Veneziani et al., 2004), as well as the relative dispersion between dif-
123 ferent particles (Piterbarg, 2002).

124 Previous applications of this hierarchy of stochastic models in the Lagrangian frame-
125 work have been restricted to the horizontal plane (e.g. Haza et al. (2007); Koszalka et
126 al. (2013)). However, dispersion through stirring in the interior occurs primarily along
127 sloping surfaces of neutral buoyancy (McDougall, 1987), which are closely related to isopyc-
128 nals (surfaces of constant potential density). Spivakovskaya et al. (2007) therefore in-
129 vestigated an isopycnal formulation of the random walk dispersion model. Shah et al. (2011)
130 and Shah et al. (2013) further investigated how the spurious diapycnal flux due to nu-
131 merical integration can best be minimized.

132 In this study, we discuss, implement, and test an isoneutral formulation of the Markov-
133 1 subgrid-scale dispersion model. We compare the Markov-0 and Markov-1 models when
134 applied to coarse-resolution and coarsened model output data. Specifically, we apply these
135 parameterizations to a channel model of the Southern Ocean, with scales and model set-
136 tings comparable to contemporary global and basin-scale ocean models. This allows us
137 to also assess the spurious dianeutral flux associated with interpolating discrete ocean
138 model output fields.

139 Furthermore, we also consider an anisotropic, shear-dependent formulation of the
140 diffusive/Markov-0 model, formulated by Le Sommer et al. (2011) (*LS* hereafter), which
141 accounts for anisotropy due to shearing and stretching brought about by mesoscale ed-
142 dies. Our aim here is to show how one of the many enhancements proposed to the Eu-
143 lerian diffusion parameterization can be extended to an isoneutral Lagrangian formula-
144 tion.

145 This study focuses on how the isoneutral form of the Markov-1 model, as well as
146 the anisotropic and shear-dependent form of the Markov-0 model, can best be implemented,
147 and to which qualitative differences they lead in the dispersion of Lagrangian particles
148 when compared to a dispersionless case and the isotropic Markov-0 parameterization.
149 We also assess errors of the parameterizations in terms of spurious diffusivities. We aim
150 to use sensible orders of magnitude for the model parameters, but parameter estimation
151 is not our final goal. We are chiefly concerned with formulating an isoneutral form of the
152 Markov-1 model, laying the groundwork for isoneutral subgrid-scale Lagrangian mod-
153 els beyond the isotropic diffusive/Markov-0 parameterization. Higher order stochastic
154 models beyond Markov-1 and extensions thereof will be left out of the scope of this pa-
155 per. These should nonetheless benefit from the ideas discussed in this paper. The ad-
156 vective effect of eddies as captured by the Gent-McWilliams parameterization (Gent &
157 McWilliams, 1990) is also not considered here.

158 This paper is structured as follows: in section 2, we give isoneutral formulations
159 of the Markov-0 and Markov-1 parameterizations, as well the anisotropic LS formula-
160 tion of the Markov-0 parameterization. Then, in section 3, we implement and apply these
161 parameterizations to Lagrangian simulations in an idealized situation, and in section 4
162 to ocean model data output. We assess the performance qualitatively and quantitatively.

163 Qualitatively, we compare individual particle trajectories and the dispersion of particles
 164 in a tracer-like patch with the dispersion in a fine-resolution eddy-resolving model. For
 165 the Markov-1 model we also look at the Lagrangian timescale and associated asymptotic
 166 diffusivity, to assess to which extent we can reproduce these profiles in a fine-resolution
 167 setting. Quantitatively, we investigate the spurious dianeutral diffusivity of the differ-
 168 ent models. These models should keep particles restricted to neutral surfaces, but since
 169 we use discrete model output, spurious dianeutral fluxes will occur due to interpolation
 170 and other numerical aspects. We wrap up this study with concluding remarks in section
 171 5.

172 2 Lagrangian isoneutral subgrid-scale models

173 2.1 Markov-0 (diffusion)

174 When we interpret the (Eulerian) advection-diffusion equation (1) as a Fokker-Planck
 175 equation that gives the probability distribution of particle locations over time (Heemink,
 176 1990), this yields a stochastic differential equation (SDE) describing the evolution of La-
 177 grangian particle positions \mathbf{x} as

$$d\mathbf{x} = [\bar{\mathbf{u}}(\mathbf{x}) + \nabla \cdot \mathbf{K}(\mathbf{x})]dt + \mathbf{V}(\mathbf{x}) \cdot d\mathbf{W}(t). \quad (2)$$

178 Here, \mathbf{V} is computed from \mathbf{K} as $\mathbf{K} = \frac{1}{2}\mathbf{V} \cdot \mathbf{V}^T$, meaning that the random noise on the
 179 particle position is proportional to the elements of the diffusivity tensor. This requires
 180 \mathbf{K} to be symmetric and positive-definite. $d\mathbf{W}(t)$ is a vector whose elements correspond
 181 to independent Wiener increments in each respective coordinate direction. These Wiener
 182 increments are normally distributed random variables $\mathcal{N}(0, dt)$ with zero mean and vari-
 183 ance dt (see also Appendix A from Shah et al. (2011)).

184 The $\nabla \cdot \mathbf{K}$ -term in (2) ensures the well-mixed condition (WMC) when the diffu-
 185 sivity tensor is not spatially uniform, and follows the interpretation of (1) as the Fokker-
 186 Planck equation corresponding to the SDE (2) (Heemink, 1990). Simply put, the well-
 187 mixed condition ensures that a particle distribution that is initially mixed, stays mixed.
 188 This condition is also essential for the forward- and backward-in-time formulations of
 189 the model to be consistent. The WMC is extensively discussed by Thomson (1987).

190 The stirring of tracers and dispersion of particles occurs primarily along sloping
 191 neutrally buoyant surfaces (McDougall, 1987). Due to uncertainty about its strength,
 192 spatial variation, and anisotropy of eddy stirring, the eddy diffusivity is often pragmat-
 193 ically chosen to be a homogeneous and isotropic in the neutral plane, with its strength
 194 expressed by the ‘diffusivity’ κ (with units $\text{m}^2 \text{s}^{-1}$). Redi (1982) showed that a diffusiv-
 195 ity tensor with these characteristics can be written in geodesic coordinates in terms of
 196 the slopes of the locally neutral plane:

$$\mathbf{K}_{\text{Redi}} = \frac{\kappa}{1 + S_x^2 + S_y^2} \begin{bmatrix} 1 + \epsilon S_x^2 + S_y^2 & -(1 - \epsilon)S_x S_y & (1 - \epsilon)S_x \\ -(1 - \epsilon)S_x S_y & 1 + S_x^2 + \epsilon S_y^2 & (1 - \epsilon)S_y \\ (1 - \epsilon)S_x & (1 - \epsilon)S_y & \epsilon + S_x^2 + S_y^2 \end{bmatrix}, \quad (3)$$

197 where $\epsilon \equiv \kappa_{\text{dia}}/\kappa$ denotes the ratio of dianeutral (diabatic) to isoneutral diffusivity, and
 198 S_x and S_y are the slopes of the neutral surfaces. When the neutral surfaces are aligned
 199 with the isopycnals, which is the case for an equation of state that is linear in salinity
 200 and potential temperature, these slopes are found as

$$S_x = -\frac{\partial \rho}{\partial x} / \frac{\partial \rho}{\partial z}, \quad S_y = -\frac{\partial \rho}{\partial y} / \frac{\partial \rho}{\partial z}. \quad (4)$$

201 Cox (1987) showed that the diffusivity tensor (3) can be simplified when these slopes
 202 are small (say $|S| = \sqrt{S_x^2 + S_y^2} < 10^{-2}$, which is generally the case in the ocean), and
 203 when ϵ is small compared to unity, so that it reduces to

$$\mathbf{K}_{\text{Redi,approx}} = \kappa \begin{bmatrix} 1 & -S_x S_y & S_x \\ S_x S_y & 1 & S_y \\ S_x & S_y & \epsilon + |S|^2 \end{bmatrix}. \quad (5)$$

204 Particle trajectories can then be computed by integrating equation (2). A κ that
 205 is constant in space and time corresponds to the idealized case of homogeneous and sta-
 206 tionary turbulence. The model has the Markovian property that successive spatial per-
 207 turbations $\mathbf{V} \cdot d\mathbf{W}(t)$ are uncorrelated. This in turn causes successive particle velocities
 208 $\mathbf{v} = \frac{\partial \mathbf{x}}{\partial t}$ to be uncorrelated as well, which is unrealistic at short timescales (i.e. $t \not\gg$
 209 T_L) (LaCasce, 2008).

210 2.2 Anisotropic Shear-dependent Markov-0

211 While the tensors (3) and (5) assume that the diffusivity is isotropic and uniform
 212 in the isoneutral plane and and time, the transport and stirring by eddies lead to effec-
 213 tive diffusivities that are highly inhomogeneous and anisotropic (McWilliams et al., 1994;
 214 Sallée et al., 2008; Nummelin et al., 2020). The spatially inhomogenous effect of eddies
 215 on viscosity is often parameterized through the Smagorinsky parameterization (Smagorinsky,
 216 1963), which relates the strength of the viscosity to the local shear of the flow based on
 217 closure of the momentum equations. This parameterization can also be used for tracer
 218 diffusion (Le Sommer et al., 2011), and has been applied for spatially-dependent (hor-
 219 izontal) random walk dispersion to parameterize eddies in Lagrangian studies (Nooteboom
 220 et al., 2020).

221 Le Sommer et al. (2011) derived an anisotropic and shear-dependent diffusion pa-
 222 rameterization that also accounts for the anisotropy in effective diffusivity due to the shear-
 223 ing and stretching effect from the resolved scales on the unresolved scales. This param-
 224 eterization, here abbreviated as *LS*, was originally proposed for parameterizing the sub-
 225 mesoscale using resolved mesoscale motions, but Nummelin et al. (2020) suggest that
 226 the LS parameterization can be applied to coarser models in which the mesoscale is not
 227 resolved.

228 The isoneutral diffusivity tensor from the LS parameterization is given by

$$\mathbf{K}_{\text{LS}} = \frac{h^2}{2}(1 + \delta^2) \begin{bmatrix} p & r & pS_x + rS_y \\ r & q & rS_x + qS_y \\ pS_x + rS_y & rS_x + qS_y & pS_x^2 + qS_y^2 + 2rS_xS_y \end{bmatrix}, \quad (6)$$

229 with $p = \sqrt{r^2 + a^2} + a$ and $q = \sqrt{r^2 + a^2} - a$. Here, $r = \frac{\partial v}{\partial x} + \frac{\partial u}{\partial y}$ is the rate of shear
 230 strain and $a = \frac{\partial u}{\partial x} - \frac{\partial v}{\partial y}$ the rate of normal strain, both in the horizontal plane. The
 231 underlying assumption is that the largest contribution to the isoneutral dispersion falls
 232 within the horizontal plane. The h -term is the horizontal filter size over which the pa-
 233 rameterization acts, and $\delta = [\frac{\partial u}{\partial x} + \frac{\partial v}{\partial y}]/\sqrt{r^2 + a^2}$ is a non-dimensional divergence pa-
 234 rameter. The filter size h is related to the size of the grid and it should be tuned through
 235 an $O(1)$, model-dependent constant C that depends on the underlying advection scheme,
 236 so $h^2 = C dx \cdot dy$. A fixed dianeutral diffusivity $\epsilon\kappa$ can be set if we approximate it as
 237 a vertical diffusivity and add it to $\mathbf{K}_{\text{LS},33}$.

238 This parameterization can readily be used in Lagrangian simulations by using \mathbf{K}_{LS}
 239 (6) for the Markov-0 model (2). The parameterization is inherently local, with each of
 240 the parameters computed on the location a Lagrangian particle (or grid cell, in the Eu-
 241 lerian case).

242

2.3 Markov-1

243

244

245

246

247

Next in the hierarchy of stochastic subgrid-scale dispersion models is the Markov-1 model, also known as the random acceleration or Langevin model (Berloff & McWilliams, 2002). The Markov-1 model adds a random forcing on particle velocities, which should be proportional to the velocity variance associated to the unresolved eddies. The model's governing equations are

$$d\mathbf{x} = [\bar{\mathbf{u}}(\mathbf{x}) + \mathbf{u}']dt, \quad (7a)$$

$$d\mathbf{u}' = [-[\boldsymbol{\theta}^{-1}(\mathbf{x})] \cdot \mathbf{u}' + \tilde{\mathbf{a}}(\mathbf{x}, \mathbf{u}')]dt + \mathbf{b} \cdot d\mathbf{W}(t). \quad (7b)$$

248

249

250

251

252

253

254

255

256

The particle location \mathbf{x} evolves through integration of the resolved mean flow $\bar{\mathbf{u}}(\mathbf{x})$ and a turbulent fluctuation \mathbf{u}' . This fluctuation evolves through the stochastic differential equation (7b). The deterministic part of this equation consists of two terms: a fading-memory term, which ensures an exponential decay in the autocorrelation of the particle's velocity, regulated through the fading-memory time tensor $\boldsymbol{\theta}$ (with time as its dimension), and a drift correction term $\tilde{\mathbf{a}}$, which ensures the well-mixed condition. The stochastic forcing term consists of the Wiener increment $d\mathbf{W}$ and the random forcing is related as $\mathbf{b}\mathbf{b}^T = 2\boldsymbol{\sigma}\boldsymbol{\theta}^{-1}$. Here, $\boldsymbol{\sigma}$ is the velocity variance tensor, which relates to the strength of the velocity fluctuations \mathbf{u}' that are to be simulated:

$$\sigma_{ij} = \langle u'_i u'_j \rangle, \quad (8)$$

257

where the angled brackets denote ensemble averages over Lagrangian trajectories.

258

The drift correction term is given by

$$\tilde{a}_i = \frac{1}{2} \frac{\partial \sigma_{ik}}{\partial x_k} - \frac{\sigma_{im}}{2} (\bar{u}_m + u'_m) \frac{\partial [\sigma^{-1}]_{ij}}{\partial x_k} u'_j. \quad (9)$$

259

See Berloff and McWilliams (2002) for further details and derivations.

260

261

262

263

264

265

266

267

268

269

The nonsingular velocity variance tensor $\boldsymbol{\sigma}$ and the fading-memory time tensor $\boldsymbol{\theta}$ are the free parameters in the Markov-1 model. They can be estimated from velocity fields in which the turbulent velocity is resolved. For the velocity variance, this is clear from equation (8). The velocity variance tensor may be anisotropic, inhomogeneous in space, and evolving over time. An obvious and useful simplification is to use a single, average velocity variance parameter ν^2 that characterizes the entire system (Koszalka et al., 2013). In this case $\boldsymbol{\sigma}$ is diagonal with its values equal to ν^2 . Alternatively, the velocity variance may be a probability distribution rather than an average value in order to account for the variance in ν^2 found within different regions of a fluid domain (Berloff & McWilliams, 2003).

270

271

272

The fading-memory time tensor $\boldsymbol{\theta}$ determines the strength of the exponential decay of the turbulent velocity \mathbf{u}' . The elements of $\boldsymbol{\theta}$ are found by integrating the Lagrangian autocorrelation $R_{ij}(\tau)$ over all time lags τ :

$$\theta_{ij} = \int_0^\infty R_{ij}(\tau) d\tau, \quad (10)$$

273

where

$$R_{ij}(\tau) = \langle u'_i(t) u'_j(t + \tau) \rangle / (\langle u'^2_i \rangle \langle u'^2_j \rangle)^{1/2}. \quad (11)$$

274

275

Like the turbulent velocity, the Lagrangian autocorrelation exhibits spatial variation in the ocean, and its anisotropy can be strongly affected by the presence of jets (Griesel et

276 al., 2010). Still, it is also useful to characterize the fading-memory time of the entire sys-
 277 tem by an average value. In a homogeneous, stationary situation without boundary ef-
 278 fects, the fading memory tensor is diagonal with its values equal to the Lagrangian in-
 279 tegral time T_L .

We characterize the dispersion of particles by the single-particle (sometimes called ‘absolute’) dispersion tensor:

$$D_{ij}(t, \mathbf{x}(\mathbf{0})) = \langle (x_i(t) - x_i(0))(x_j(t) - x_j(0)) \rangle. \quad (12)$$

280 Berloff et al. (2002) note that while the dispersion tensor in the ocean may evolve in a
 281 nonlinear manner, it can be described by different power laws at intermediate timescales:

$$D_{ii}(t) \sim t^{\alpha_{ii}}. \quad (13)$$

282 Single-particle dispersion in the ocean is initially ballistic, meaning $D(t) \sim t^2$ for $t \ll$
 283 T_L . At longer time-scales, it becomes approximately linear in time, i.e. $D(t) \sim t$. Since
 284 such behavior is equivalent to that of a diffusive process, this is also referred to as the
 285 diffusive limit. Unsurprisingly, dispersion simulated by the Markov-0 model is purely dif-
 286 fusive. The Markov-1 model, however, is able to also simulate the initially ballistic be-
 287 havior of particles dispersion. For time scales longer than those characterized by the el-
 288 ements of $\boldsymbol{\theta}$, the Markov-1 model essentially behaves diffusively (Rodean, 1996). In this
 289 limit, assuming homogeneity, stationarity, and absence of boundary effects, we can re-
 290 late the absolute diffusivity, velocity variance and Lagrangian integral time as

$$\nu^2 T_L = \kappa. \quad (14)$$

291 At intermediate time-scales, α_{ii} can take on other values than 1 and 2, which is referred
 292 to as anomalous dispersion (LaCasce, 2008). While the dispersion regimes other than
 293 the ballistic and diffusive cannot be simulated by Markov-1, the higher order Markov-
 294 2 and Markov-3 models, or modifications of Markov-1 are able to account for such be-
 295 havior, such as the oscillatory component of the Lagrangian autocorrelation (Berloff &
 296 McWilliams, 2002; Reynolds, 2002; Veneziani et al., 2005). However, we limit ourselves
 297 here to Markov-1 for its simplicity, as each modification or higher model in the hierar-
 298 chy includes more free parameters.

299 We now formulate an ad-hoc three-dimensional, isoneutral version of the Markov-
 300 1 model in the case of homogeneous and stationary turbulence without boundary effects.
 301 First, we assume that the turbulent velocity perturbations should remain primarily re-
 302 stricted to the local neutral plane, in which it is isotropic. In isoneutral coordinates this
 303 yields

$$\boldsymbol{\sigma}_{\text{iso}} = \begin{bmatrix} \nu^2 & 0 & 0 \\ 0 & \nu^2 & 0 \\ 0 & 0 & \eta\nu^2 \end{bmatrix}, \quad \text{and} \quad \boldsymbol{\theta}_{\text{iso}} = \begin{bmatrix} T_L & 0 & 0 \\ 0 & T_L & 0 \\ 0 & 0 & \varepsilon T_L \end{bmatrix}. \quad (15)$$

304 Assuming there is some dianeutral velocity perturbation ν_{dia}^2 ($\ll \nu^2$), we define $\eta \equiv \nu_{\text{dia}}^2/\nu^2$.
 305 Similarly, assuming a separate dianeutral Lagrangian integral time $T_{L,\text{dia}}$, we define $\varepsilon \equiv$
 306 $T_{L,\text{dia}}/T_L$.

307 Then, we simply transform $\boldsymbol{\sigma}$ and $\boldsymbol{\theta}$ from isoneutral coordinates to geodesic coor-
 308 dinates in analogy to Redi’s formulation of the isoneutral diffusivity tensor (Redi, 1982).
 309 This yields:

$$\boldsymbol{\sigma}_{\text{geo}} = \frac{\nu^2}{1 + S_x^2 + S_y^2} \begin{bmatrix} 1 + \eta S_x^2 + S_y^2 & -(1 - \eta) S_x S_y & (1 - \eta) S_x \\ -(1 - \eta) S_x S_y & 1 + S_x^2 + \eta S_y^2 & (1 - \eta) S_y \\ (1 - \eta) S_x & (1 - \eta) S_y & \eta + S_x^2 + S_y^2 \end{bmatrix}, \quad (16)$$

310 and

$$\boldsymbol{\theta}_{\text{geo}} = \frac{T_L}{1 + S_x^2 + S_y^2} \begin{bmatrix} 1 + \varepsilon S_x^2 + S_y^2 & -(1 - \varepsilon)S_x S_y & (1 - \varepsilon)S_x \\ -(1 - \varepsilon)S_x S_y & 1 + S_x^2 + \varepsilon S_y^2 & (1 - \varepsilon)S_y \\ (1 - \varepsilon)S_x & (1 - \varepsilon)S_y & \varepsilon + S_x^2 + S_y^2 \end{bmatrix}. \quad (17)$$

311 Note that in order for these tensors to be nonsingular, η and ε should be nonzero, mean-
 312 ing that $\boldsymbol{\sigma}_{\text{geo}}$ and $\boldsymbol{\theta}_{\text{geo}}$ have nonzero diapycnal contributions. We thus have to specify
 313 η and ε in a way such that they are small enough to prevent large dianeutral excursions.

314 While the diffusivity tensor (3) can be simplified (5) by the assumption that slopes
 315 are small, this assumption cannot be applied to the tensors $\boldsymbol{\sigma}_{\text{geo}}$ (16) and $\boldsymbol{\theta}_{\text{geo}}$ (17), since
 316 the terms that are scaled out in the small-slope assumption become dominant in the in-
 317 verses of $\boldsymbol{\sigma}_{\text{geo}}$ and $\boldsymbol{\theta}_{\text{geo}}$, which are used in (7), (9) and when computing \mathbf{b} .

318 A key assumptions of Redi's diffusivity tensor \mathbf{K}_{redi} is that the neutral surfaces are
 319 stationary and locally flat. 'Locally' here is related to the length scale associated to the
 320 displacement of a particle over one timestep. The assumption is that when a particle is
 321 advected, the neutral slope at the particle's original location \mathbf{x}_0 at time t_0 is approxi-
 322 mately equal to the neutral slope at the particle's new location \mathbf{x}_1 after a timestep dt .
 323 Any difference in the orientation of the neutral surface over successive timesteps will lead
 324 to some dianeutral movement, but as long as neutral surfaces are locally flat, this dia-
 325 neutral movement is limited and the new local slopes are used for computing the next
 326 neutral displacement.

327 For Markov-1, the situation is more complicated. In this case, the stochastic ve-
 328 locity perturbations of a particle at time t_0 and location \mathbf{x}_0 are oriented parallel to the
 329 local neutral plane. However, since particle velocities (7b) are autocorrelated, the cur-
 330 vature of the neutral surface at a particle's initial location \mathbf{x}_0 can influence a particle's
 331 velocity over several timesteps, as the particle is displaced away from \mathbf{x}_0 . This influence
 332 decays exponentially with the e -folding timescale εT_L . Thus if a neutral surface curves
 333 at spatial scales that are similar to or smaller than the length scale L over which a par-
 334 ticle travels within the timescale εT_L , the signal of the turbulent velocity perturbation
 335 at t_0 influences the particle's net turbulent velocity, causing a dianeutral velocity con-
 336 tribution, and therefore a dianeutral displacement. To combat this dianeutral movement,
 337 the Lagrangian autocorrelation in the dianeutral direction should rapidly decay away at
 338 each timestep. Put differently, εT_L should be so small that a neutral surface can be ap-
 339 proximated as flat over the length scale L . While εT_L should be larger than zero to avoid
 340 singularity of $\boldsymbol{\theta}$, one ad-hoc workaround to rapidly extinguish the signal of velocity per-
 341 turbations at previous timesteps is to set

$$\varepsilon T_L = dt. \quad (18)$$

342 This workaround comes at a price: if the neutral surface curves, the Lagrangian decor-
 343 relation of an initially isoneutral signal may occur more quickly than is prescribed by
 344 $\boldsymbol{\theta}$, since the initially isoneutral perturbation becomes dianeutral over time, which causes
 345 it to decay rapidly due to (18). This effect increases when more curvature is covered by
 346 a Lagrangian particle as it moves in space and time. Properly retaining autocorrelations
 347 on curved surfaces is a complicated matter (Gaspari & Cohn, 1999), so here we take a
 348 pragmatic approach by assuming that the change in isoneutral curvature is small enough
 349 for practical use to warrant our ad-hoc formulation of a three-dimensional Markov-1 model.

350 Finally, when ε is fixed by (18), η can be chosen in such a way that the effective
 351 dianeutral diffusivity in the limit $t \gg T_L$ is controlled as:

$$\epsilon \kappa = \eta \nu^2 \varepsilon T_L. \quad (19)$$

352 This means that if we indeed assume homogeneity, stationarity, and a lack of boundary
 353 effects, the parameters necessary for Markov-1 model may be determined by specifying
 354 the Lagrangian integral time T_L and an effective diffusivity κ , which fix ν^2 through (14),
 355 and by specifying the dianeutral diffusivity ratio ϵ , fixing ε and η (through (18) and (19)).

356 **3 Numerical implementation**

357 **3.1 Discretization**

To use the Markov-0 and Markov-1 models numerically, we need to discretize SDEs (2) and (7). The simplest SDE discretization is Euler-Maruyama scheme, which can be seen as a stochastic version of the Euler-forward scheme. Given a general stochastic differential equation

$$d\mathbf{X} = \alpha(\mathbf{X}, t)dt + \beta(\mathbf{X}, t)d\mathbf{W}(t), \quad (20)$$

358 with $\alpha(\mathbf{X}, t)$ signifying the deterministic forcing strength and $\beta(\mathbf{X}, t)$ the stochastic forcing
 359 strength, the Euler-Maruyama scheme approximates the true solution for X by the
 360 Markov chain Y as

$$Y_{n+1}^k = Y_n^k + \alpha^k \Delta t + \sum_{j=1}^m \beta^{k,j} \Delta W^j, \quad (21)$$

361 where superscripts denote the k -th component of the m -dimensional vectors \mathbf{X} and \mathbf{Y}
 362 and subscripts denote discrete time indices. $\Delta\mathbf{W}$ is an m -dimensional vector of discretized
 363 Wiener increments, which are normally distributed, $\mathcal{N}(0, \Delta t)$, with zero mean and vari-
 364 ance Δt . See Kloeden and Platen (1999) or Iacus (2008) for more details on numerical
 365 SDE schemes. The expressions for α and β can be readily identified in (2) and (7b). In
 366 the case of Markov-1, an additional numerical integration is necessary for (7a). For con-
 367 sistency with the Euler-Maruyama scheme, this can simply be the Euler-Forward dis-
 368 cretization.

369 We implemented the Markov-0 and Markov-1 schemes in the *Parcels* Lagrangian
 370 framework (Delandmeter & van Sebille, 2019). All Lagrangian simulations in this pa-
 371 per are carried out with *Parcels* (van Sebille et al., 2020).

372 **3.2 Idealized test case**

373 We assess the validity of the isoneutral subgrid-scale models using an idealized, sta-
 374 tionary density field for which we can compute the isoneutral slopes exactly, assuming
 375 that here the neutral surfaces align with the isopycnals. We do not consider any actual
 376 fluid dynamical setup, meaning there is no background flow ($\bar{\mathbf{u}} = 0$). This three-dimensional
 377 idealized test case is an extension of the two-dimensional test case from Shah et al. (2011),
 378 and is given by

$$\rho(x, y, z) = \rho_0 \left[1 - \frac{N^2 z}{g} + A_x \sin(k_x x) + A_y \sin(k_y y) \right], \quad (22)$$

379 with ρ_0 a reference density, N the Brunt-Vaisala frequency, g the gravitational acceler-
 380 ation, A the amplitude of the wave-like neutral surfaces, and k their wavenumber (sub-
 381 scripts denoting direction). The z -coordinate of the neutral surface corresponding to the
 382 density ρ^* is then found as

$$z_{\text{iso}}(\rho^*, x, y) = \frac{g}{N^2} \left[1 - \frac{\rho^*}{\rho_0} + A_x \sin(k_x x) + A_y \sin(k_y y) \right]. \quad (23)$$

We use a similar choice of parameters as (Shah et al., 2011), which is representative of the large-scale ocean:

$$\begin{aligned} \rho_0 &= 1025 \text{ kg m}^{-3}, & N^2 &= 10^{-5} \text{ s}^{-2}, & g &= 10 \text{ m s}^{-2}, \\ A_x &= 1 \times 10^{-3}, & A_y &= 1.1 \times 10^{-3}, & k_x &= k_y = \frac{2}{\pi} \times 10^{-5} \text{ m}^{-1}. \end{aligned} \quad (24)$$

This choice of parameters leads to a maximum slope of $\max(|S|) \approx 10^{-3}$, which is a typical value for neutral slopes in the ocean, and for which the small-slope approximation (5) is valid (Mathieu & Deleersnijder, 1998).

3.3 Spurious diffusivity

We can compare the spurious dianeutral diffusivities induced by numerical errors in the discretized Markov-0 and Markov-1 models. We limit this analysis for brevity and refer the reader to Shah et al. (2011) for an extensive discussion of numerical errors introduced by Markov-0. The models considered here have an equivalent effective diffusivity (14) in the limit $t \gg T_L$. We initialize 1250 particles on a neutral surface, using a regular x, y -grid, with their z -coordinate computed from (23) and $\rho^* = 1027.5 \text{ kg m}^{-3}$. We found that results are insensitive to adding more particles. We take into account the periodic topology of the neutral surfaces to make sure crests and troughs are sampled evenly. Then, we numerically integrate the particles for 90 days using several choices of integration timestep Δt . The particle displacements are computed by using the exact density field (22) and its spatial derivatives. From the vertical departure of the particles from the neutral surfaces, we can compute an effective spurious vertical diffusivity,

$$\kappa_{z,\text{spurious}} = \frac{\langle (z - z_{\text{iso}}) \rangle^2}{2T_{\text{int}}}, \quad (25)$$

where the angled brackets denote a particle ensemble average and T_{int} is the total integration time. We use this as an approximation of the spurious dianeutral diffusivity introduced by the numerical approximation of (20).

In the Markov-0 model, we set $\kappa = 1000 \text{ m}^2 \text{ s}^{-1}$ and $\epsilon = 0$, such that the only dianeutral movement of particles is due to numerical errors. We test both \mathbf{K}_{Redi} and $\mathbf{K}_{\text{Redi,approx}}$. We cannot test Markov-0 using \mathbf{K}_{LS} , as we do not consider a fluid setup with flow from which the parameters are computed.

For Markov-1, we use a value of $T_L = 20$ days, and we determine $\nu^2 = \kappa/T_L = 5.79 \times 10^{-4} \text{ m}^2 \text{ s}^{-2}$, so that the effective isoneutral diffusivity in the diffusive limit equals the one used for Markov-0 (see (14)). We also need to specify the nonzero dianeutral fading-memory time and velocity variance in the Markov-1 model to guarantee that (16) and (17) are nonsingular. To ensure rapid decorrelation of \mathbf{u}' in the local dianeutral direction, we set $\varepsilon = \frac{\Delta t}{T_L}$ (18). In order to avoid $\boldsymbol{\theta}$ being singular, we also need a nonzero η . However, here we are interested in the dianeutral movement induced by numerical errors, rather than what is specified by the algorithm. We choose $\eta = 10^{-10}$ and will show that it is sufficiently small so that the numerical errors dominate the dianeutral diffusivity. This then allows us to compare the errors between both Markov models.

Figure 1 shows that the spurious dianeutral diffusivity after 90 days of integration is much smaller for Markov-1 than for Markov-0. Recall that both use the same Euler-Maruyama discretization scheme (21). The difference in dianeutral diffusivity is due to the fact that the expected turbulent displacement for a single timestep in Markov-1 is $E(\|\mathbf{u}'\| \Delta t) = \nu \Delta t$ (see (7)), while that in Markov-0 is $E(\mathbf{V} \cdot d\mathbf{W}) = \sqrt{2\kappa \Delta t}$, (see (2)) where E denotes the expected value and $\|\cdot\|$ the vector norm. The turbulent excursion of Markov-1 in one timestep is therefore much smaller than that of Markov-0 over the range of Δt investigated here, and thus Markov-1 introduces less dianeutral movement as the neutral surfaces curve. Also note that over this range of Δt and with our

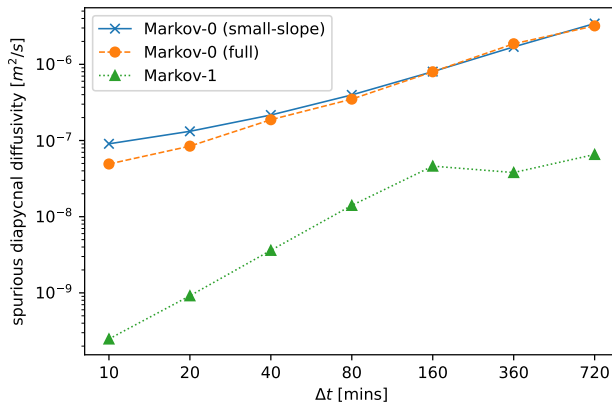


Figure 1. Spurious diapycnal diffusivities after 90 days in the Markov-0 model (with and without the small-slope approximation (5)), and the Markov-1 model, using several timesteps Δt . The Markov-1 model has a much smaller spurious diapycnal flux for each timestep. Using the small-slope approximation in the Markov-0 model does not seem to impact the error much.

425 choice of κ , ε and η , the hypothetical diapycnal diffusivity of Markov-1 should be smaller
 426 than the diapycnal diffusivities seen in Figure 1. This means that the numerical error
 427 here dominates the explicitly set diapycnal diffusivity, allowing us to properly compare
 428 the numerical errors introduced by Markov-0 and Markov-1.

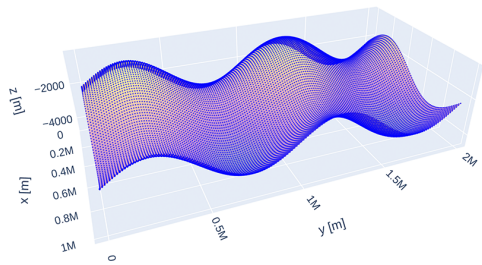
429 Several studies propose the use of higher order numerical schemes to reduce the spu-
 430 rious diapycnal flux resulting from numerical integration (Shah et al., 2011; Gräwe, 2011;
 431 Gräwe et al., 2012) or the use of adaptive time-stepping methods (Shah et al., 2013). While
 432 higher order schemes, such as the first order Milstein scheme (see Kloeden & Platen, 1999),
 433 indeed perform better in the idealized configuration, we find that this improvement is
 434 negligible when applied to discrete ocean model data using commonly used spatial and
 435 temporal output resolutions (see section 4.1), and a Lagrangian timestep of 40 minutes,
 436 indicating that the error introduced by interpolating Eulerian data dominates that of
 437 the numerical method.

438 3.4 Well-mixedness

439 The equations for the Markov-1 model, including the drift-correction term (9), have
 440 been rigorously derived by Berloff and McWilliams (2002). However, since we create an
 441 ad-hoc adaptation of this model for use in three-dimensional isoneutral situations, it is im-
 442 portant that we verify whether we did not inadvertently violate the well-mixed condi-
 443 tion. Rather than rigorously proving the WMC, we take a pragmatic approach here and
 444 visually inspect particle distributions to see if we can find spurious accumulation. We
 445 choose pragmatism over rigor of proof, because in applications with discrete Eulerian ocean
 446 model output, Lagrangian simulations with Markov-0 and Markov-1 are both affected
 447 by numerical errors due to discretization and interpolation. These numerical aspects will
 448 violate the WMC in any case, hence a pragmatic visual verification of the WMC satis-
 449 fies our needs.

450 To visually inspect any spurious particle accumulation, which would indicate a WMC-
 451 violation, we integrate 12,800 particles with the Markov-0 and Markov-1 models for 90
 452 days and investigate particle distributions. Figure 2 shows the initial and final particle
 453 distributions on our idealized neutral surfaces for Markov-1. We again set $T_L = 20$ days
 454 and $\nu^2 = \kappa/T_L \approx 5.79 \times 10^{-4} m^2 s^{-2}$, so that the effective diffusivity after 90 days (in

a) Initialized particles



b) Markov-1 after 90 days

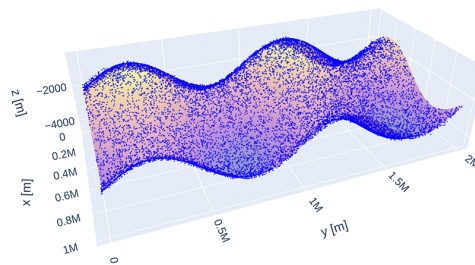


Figure 2. a) 12,800 particles on an idealized neutral surface, initialized in a regular xy -grid. b) the same particles after 90 days of integration with the Markov-1 model, with $T_L = 20$ days and $\nu^2 = 5.79 \times 10^{-4} \text{ m}^2 \text{ s}^{-2}$. Particles remain close to the neutral surface they were released on. We do not observe any distinct zones in which particles accumulate.

455 the diffusive limit) is approximately $\kappa \approx 1 \times 10^3 \text{ m}^2 \text{ s}^{-1}$. We do not observe any dis-
 456 tinct zones in which particles accumulate. Since the input to the Markov-1 model in this
 457 test case solely consists of the σ and θ tensors, whose elements in turn depend on the
 458 slopes of the neutral surfaces, any spurious accumulation should manifest itself at spe-
 459 cific slope levels. Since we do not observe this, this indicates that in this stationarity sit-
 460 uation without background flow the WMC is not violated by our ad-hoc isoneutral for-
 461 mulation of Markov-1.

462 4 Dispersion in an Antarctic Circumpolar Current Channel Model

463 We also compare the Markov-0 and Markov-1 models through Lagrangian simu-
 464 lations using the output of an ocean model. We use two types of Eulerian model fields
 465 at a 50 km horizontal spacing: one is the output of an ocean model run at this *coarse*
 466 resolution, and the other is a *coarsened* output of a *fine-resolution* 5 km model. The fine-
 467 resolution data serves as an eddy-resolving reference case. While the coarse-resolution
 468 data is most representative of the coarse models for which Lagrangian subgrid-scale mod-
 469 els are useful, the coarsened data allows for easier comparison to the fine-resolution ref-
 470 erence case.

471 First, we look at how well Markov-1 reproduces the specified Lagrangian integral
 472 timescale and effective diffusivity in the diffusive limit. Then, we qualitatively compare
 473 particle trajectories produced by Markov-0 and Markov-1 with those produced by ad-
 474 vection only. We also compare the spread of a patch of Lagrangian particles, in analogy
 475 to a tracer patch experiment. Finally, we estimate the spurious dianeutral diffusivities
 476 introduced by the different models.

477 In each experiment, we use single values for the isoneutral Lagrangian integral time
 478 and isoneutral velocity variance. This means that we assume a homogeneous and sta-
 479 tionary situation without boundary effects. The stationarity assumption is valid for the
 480 coarsened and coarse fields, but the other assumptions are not. To deal with inhomog-
 481 eneity, we could use space-dependent and anisotropic tensors for σ and θ , but since fu-
 482 ture applications are likely to use constant parameters, we choose the pragmatic route
 483 and do so as well.

484 Since we use Eulerian data with boundaries, we need to consider boundary con-
 485 ditions. In a two-dimensional stationary and homogeneous setting, perfect reflection sat-
 486 isfies the WMC (Wilson & Flesch, 1993). Although neutral surfaces in the Southern Ocean

487 can outcrop at the surface (Marshall & Speer, 2012), we use the assumption that neu-
 488 tral slopes at the lateral boundaries are near-flat, and adopt perfect reflection as our choice
 489 as well. The isoneutral slopes in certain areas of the model data may be unrealistically
 490 large due to spurious effects, so we use a tapering scheme based on that of Danabasoglu
 491 and McWilliams (1995) to lower or turn off turbulent displacements in such regions. De-
 492 tails of the tapering mechanism are found in supporting information Text S1.

493 4.1 Eulerian model description

494 We use a simplified model of the Antarctic Circumpolar Current run in MITgcm
 495 (Marshall et al., 1997; Campin et al., 2020), similar to the channel model used by Abernathey
 496 et al. (2011) and Balwada et al. (2018). We use an adaptation that is extensively described
 497 in MITgcm’s documentation, also available at: [https://mitgcm.readthedocs.io/en/
 498 latest/examples/reentrant_channel/reentrant_channel.html](https://mitgcm.readthedocs.io/en/latest/examples/reentrant_channel/reentrant_channel.html). It consists of a zon-
 499 ally re-entrant channel that is 1000 km long in the zonal (x) direction, 2000 km wide in
 500 the meridional (y) direction, and 3980 m deep. The model consists of 49 vertical levels
 501 that range from 5.5 m depth at the surface to 149 m at depth. It is forced by a constant
 502 sinusoidal wind stress and a temperature relaxation at the surface and northern bound-
 503 ary. The equation of state is set linearly dependent to potential temperature only, caus-
 504 ing the neutral surfaces to coincide with surfaces of constant potential temperature. This
 505 allows us to compute neutral slopes using (4). To break zonal symmetry, a meridional,
 506 Gaussian-shaped ridge is placed in the center of the domain, going up to 2382.3 m depth.
 507 The ridge has a small opening in the center, causing a strong barotropic jet to develop.

508 The model is spun up for 100 years and run at two horizontal resolutions: once at
 509 5 km resolution (*fine-resolution*), at which the mesoscale eddies are resolved, and once
 510 at 50 km resolution (*coarse-resolution*) where eddies cannot develop. Daily averages of
 511 the output data are used for the Lagrangian simulations. The coarse-resolution flow is
 512 in steady-state, exhibiting no temporal variability. We also create a coarsening of the
 513 fine-resolution model in space and time, by taking a yearly time-average of the flow and
 514 spatially averaging velocities and temperature fields over 50 kilometers. These coarsened
 515 fields thus include the effect of eddies on the mean flow. Snapshots and means of the vor-
 516 ticity and speed fields in the fine, coarsened and coarse runs are found in Figure S1. The
 517 derivatives of the density field, used for computing the neutral slopes, are computed by
 518 means of grid-aware central differences using the *XGCM* package (Abernathey et al., 2021).

519 4.2 Parameter estimation

520 To use the two Markov models in our experiments, we need to identify κ for Markov-
 521 0 (except when using the LS parameterization) and T_L and ν^2 for Markov-1. We can es-
 522 timate globally representative values from Lagrangian quantities of the fine-resolution
 523 flow field. To do so, we first compute Lagrangian particle trajectories with the fine-resolution
 524 model output. We initialize 64,860 Lagrangian particles released regularly spaced apart
 525 20 km in the horizontal and 200 m in the vertical, with $-200 \text{ m} \geq z \geq -1600 \text{ m}$ in or-
 526 der to stay away from the mixed layer and the ridge. We then integrate the trajectories
 527 using a 4th order Runge-Kutta scheme, with a timestep $\Delta t = 40$ minutes for 180 days.

528 The Lagrangian integral time is related to the Lagrangian autocorrelation (11). Fig-
 529 ure 4 shows the Lagrangian autocorrelation estimated from particle trajectories in the
 530 fine-resolution model. We can clearly see the oscillatory and exponentially decaying be-
 531 havior of the horizontal autocorrelations. Similar to Sallée et al. (2008), we approximate
 532 the Lagrangian autocorrelation to be decomposable as

$$R(\tau) = \cos(2\pi\Omega) e^{-\tau/T_L}, \quad (26)$$

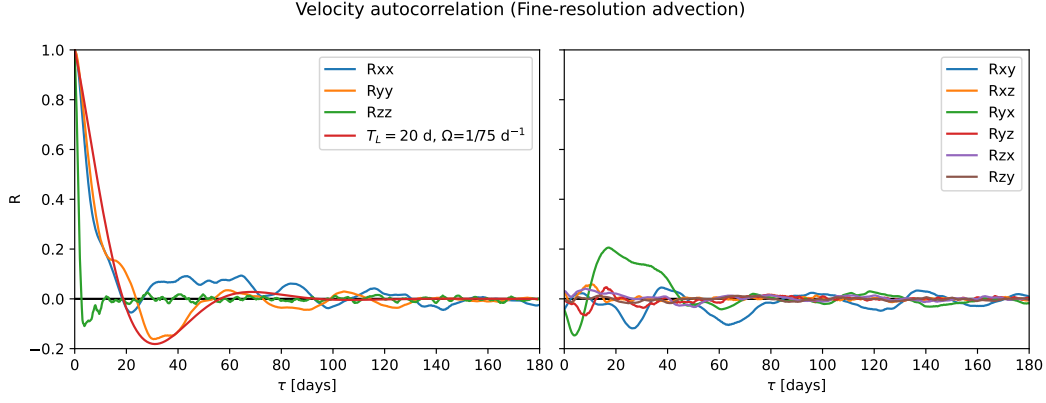


Figure 3. Lagrangian autocorrelations in the fine-resolution model, including an exponentially decaying and oscillatory function (26) with $T_L = 20$ days and $\Omega = 75$ days.

533 where Ω is the frequency of the oscillation. While the parameters T_L and Ω can be es-
 534 timated using a least-square fit, we are only interested in approximate values for the pa-
 535 rameters. A choice of $\Omega = 1/75$ per day and $T_L = 20$ days approximates the auto-
 536 correlation functions well enough for our purposes. Bear in mind, though, that we only
 537 continue with T_L , as Markov-1 cannot reproduce the oscillatory behavior of particle dis-
 538 persion in the ocean.

539 Having fixed T_L , we only need to estimate κ , since this will readily give us an av-
 540 erage value of ν^2 that reproduces the correct diffusivity in the dispersive regime through
 541 (14) (Koszalka et al., 2013). The absolute diffusivity tensor (LaCasce, 2008) is found by
 542 integrating the Lagrangian autocovariance:

$$K_{ij}(\mathbf{x}, \tau) = \int_0^\tau \langle u'_i(t_0|\mathbf{x}, t_0)u'_j(t_0 + \tilde{\tau}|\mathbf{x}, t_0) \rangle d\tilde{\tau}. \quad (27)$$

543 To find the isoneutral diffusivities, i and j should coincide with the principal directions
 544 of the neutral plane at each location. However, since the isoneutral slope in our model
 545 is small (generally of order 10^{-3}), we will estimate the isoneutral diffusivity from K_{xx}
 546 and K_{yy} .

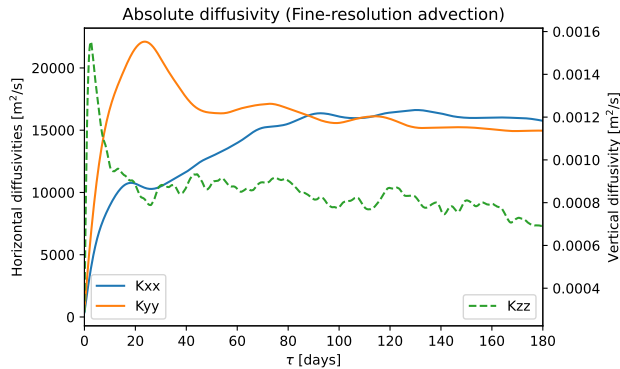


Figure 4. Absolute diffusivities K_{xx} , K_{yy} , and K_{zz} , in the fine-resolution model, computed through (27).

547 Figure 4 shows the horizontal and vertical absolute diffusivities over time. The absolute
 548 diffusivity corresponding to the diffusive limit, in which Markov-0 is valid, is found
 549 at $\tau \gg T_L$, for which the diffusivity should take on a near-constant value. Theoretically,
 550 it is found by integrating (27) to infinity, but in practice, it can be found by integrating
 551 past the negative and positive lobes associated with the oscillatory component of the
 552 Lagrangian autocorrelation, when the diffusivity becomes near-constant (Klocker,
 553 Ferrari, Lacase, & Merrifield, 2012; Griesel et al., 2014). From Figure 4, we estimate
 554 the isoneutral diffusivity to be similar to the horizontal absolute diffusivity, with a value
 555 of $\kappa = 1.5 \times 10^4 \text{ m}^2 \text{ s}^{-1}$.

556 4.3 Lagrangian integral time and diffusivity from the Markov-1 model

557 Now we initialize particles in the same lattice as used in section 4.2 and apply the
 558 Markov-1 parameterization. We simulate trajectories by integrating the stochastic differential
 559 equations (7) using the Euler-Maruyama scheme (21) for 180 days, with $\Delta t =$
 560 40 minutes. We set $T_L = 20$ days, and specify $\nu^2 = 8.68 \times 10^{-3} \text{ m}^2 \text{ s}^{-2}$ in order to obtain
 561 an effective diffusivity of $1.5 \times 10^4 \text{ m}^2 \text{ s}^{-1}$ in the diffusive limit. We also set η and
 562 ε in such a way that the effective diapycnal diffusivity in the limit $t \gg T_L$ is $1 \times 10^{-5} \text{ m}^2 \text{ s}^{-1}$.
 563 These settings are used in the remainder of this study. Derivatives of Eulerian quantities
 564 that are necessary for computing the tensor elements of σ and θ (and later \mathbf{K}) are
 565 computed with central differences and successively interpolated linearly in space. Our
 566 aim is to see how well the model reproduces the diffusivity and Lagrangian timescale that
 567 we specified, to verify our ad-hoc diapycnal formulation of Markov-1.

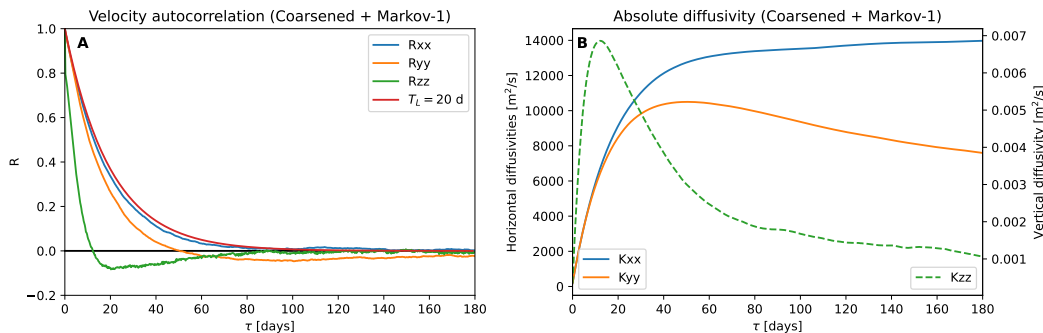


Figure 5. Lagrangian autocorrelation and absolute diffusivity produced by the Markov-1 model when applied on the coarsened field. The Lagrangian autocorrelation in the x -direction best resembles that of an exponentially decaying function with a 20-day e -folding timescale (in red for reference).

568 Figure 5 shows the Lagrangian autocorrelation and absolute diffusivity of particles
 569 simulated using the Markov-1 subgrid-scale model using the coarsened field, similar
 570 to Figures 3 and 4. Figure S2 provides a similar diagram for the coarse field. The
 571 exponential decay with an e -folding timescale of 20 days can be clearly seen in the
 572 autocorrelation. There is a clear absence of the oscillatory component, which Markov-1 is
 573 unable to simulate.

574 The absolute diffusivity of $1.5 \times 10^4 \text{ m}^2 \text{ s}^{-1}$ is not fully reproduced. In the x -direction,
 575 values reach up to approximately $1.4 \times 10^4 \text{ m}^2 \text{ s}^{-1}$, but in the y -direction, they are much
 576 lower, with a maximum of $1.0 \times 10^4 \text{ m}^2 \text{ s}^{-1}$ and a decrease at larger time lags. There are
 577 two reasons why values do not reach $1.5 \times 10^4 \text{ m}^2 \text{ s}^{-1}$. First, in regions where the slope
 578 is unrealistically high, turbulent velocities are tapered to zero (see supporting information
 579 Text S1), which decreases the absolute diffusivity computed from the particle en-

580 semble. Second, the lateral domain boundaries limit the dispersion of material and there-
 581 fore also cause a decrease in diffusivity, as D_{yy} cannot grow linearly over long timescales.
 582 While the effect of tapering likely plays a role for both K_{xx} and K_{yy} , only K_{yy} is affected
 583 by boundaries, which causes it to decrease over time. We clearly see that R_{zz} has a much
 584 shorter e -folding time than 20 days. This is likely due to the effect of curvature in the
 585 neutral surfaces, and the rapid decorrelation we impose in the dianeutral directions (18).

586 4.4 Individual trajectories

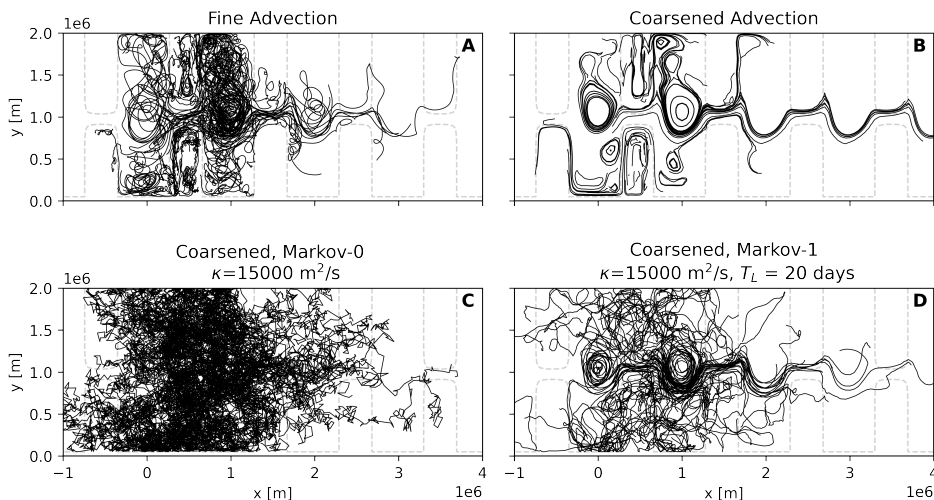


Figure 6. 100 randomly subsampled trajectories from 180 days of simulation on (a) fine-resolution and (b) coarsened fields, and using coarsened fields in combination with (c) the diffusive parameterization and (d) Markov-1. While the domain is periodic, here we tile it in the zonal direction, to separate particles crossing the zonal periodic boundaries. The -3900m isobath is plotted with dashed grey lines, indicating the location of the ridge in the periodic channel.

587 A typical aim of Lagrangian subgrid-scale dispersion models is to construct real-
 588 istic synthetic particle pathways in the absence of turbulent eddies. It is therefore illus-
 589 trative to plot particle trajectories generated by advection using the three model fields
 590 (fine, coarsened and coarse) and compare those with trajectories generated by Markov-
 591 0 and Markov-1. To do so, we randomly subsample 100 trajectories that were initialized
 592 on the same lattice as used in section 4.2. We again use the Runge-Kutta 4 scheme for
 593 advection and Euler-Maruyama for the Markov models, a timestep $\Delta t = 40$ minutes,
 594 and a simulation time of 180 days. Like in the previous section, we tuned Markov-1 to
 595 produce a diapycnal diffusivity of $1 \times 10^{-5} \text{ m s}^{-1}$, and now we do the same for Markov-
 596 0 by setting $\epsilon\kappa$ accordingly. These parameters will also be used for the remainder of this
 597 paper. To more easily identify re-entering trajectories, we record when particles cross
 598 the periodic boundary, so that we can plot particle trajectories as unbroken paths by re-
 599 peating the periodic domain in the zonal direction.

600 Figure 6 considers 100 trajectories from Markov-0 and Markov-1 in the coarsened
 601 case, compared to advection using fine-resolution and coarsened fields, which serve as
 602 reference. These trajectories are released at different horizontal and vertical locations,
 603 subsampled from the lattice used in the previous two sections. From the trajectories in
 604 Markov-0 we clearly see that there is no autocorrelation in the particle velocities, with
 605 the directions in which a particle moves rapidly changing between recorded timesteps.
 606 Particles simulated with Markov-0 also travel much more, as the turbulent displacement

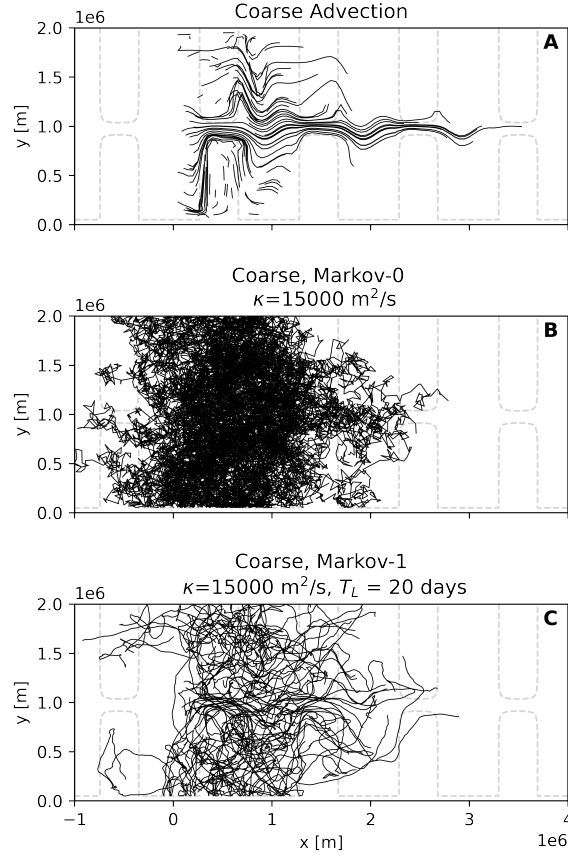


Figure 7. Same as Figure 6, but using coarse-resolution fields.

607 in this model is much larger than that of Markov-1 (see the discussion in section 3.3).
 608 Markov-1 clearly does a better job at simulating the trajectories from the fine-resolution
 609 reference run. A major difference is that trajectories in the fine run exhibit looping mo-
 610 tions. While the trajectories in Markov-1 veer over time, it is unable to produce the loop-
 611 ing motions that are seen in the fine-resolution run (Veneziani et al., 2005). Bear in mind
 612 that in the stochastic perturbations between different particles advected by Markov-0
 613 and Markov-1 are uncorrelated. Instead, each particle ‘feels’ its own turbulent field.

614 Figure 7 considers the coarse-resolution case. In this case, the underlying flow field
 615 has no eddies. When comparing trajectories produced by the Markov models, we thus
 616 have no eddying reference case. In the advection-only case, the absence of strong dis-
 617 persion is clear. One major difference with the results from the coarsened case is the ab-
 618 sence of any stationary meanders. Trajectories produced by Markov-1 again seem the
 619 most realistic when compared to Figure 6a, albeit less obviously than was the case for
 620 6d.

621 **4.5 Tracer spread**

622 In analogy to studying the spread of a small patch of tracer (Wagner et al., 2019),
 623 we qualitatively compare the spread of a patch of Lagrangian particles advected in the
 624 fine-resolution, coarsened, and coarse-resolution fields and apply the Markov-0 and Markov-
 625 1 subgrid-scale models to the later two flows. For Markov-0, we use the isotropic isoneu-

626 tral diffusion tensor $\mathbf{K}_{\text{Redi,approx}}$ (5) and the LS parameterization \mathbf{K}_{LS} (6). For the LS
 627 parameterization, we set $C = 1$.

628 We initialize a patch of particles initially located at $z = -736$ m (corresponding
 629 to the 25th vertical level) in a radius of 50 km centered around $(x = 250 \text{ km}, y = 1000 \text{ km})$,
 630 see Figure 8a.

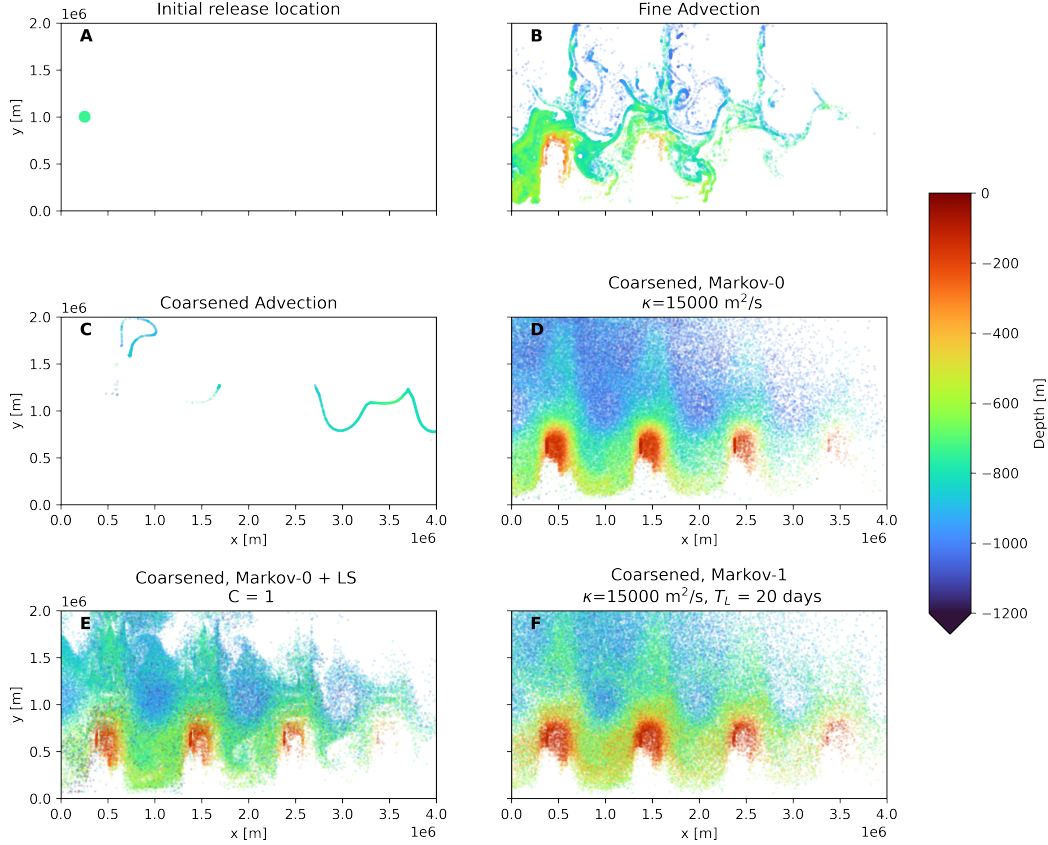


Figure 8. (a) Initial particle positions at $z = -736$ m, (b)-(f) show particle locations and depths after 180 days of simulation with $\Delta t = 40$ minutes. (b) & (c) show particles advected with the fine-resolution and coarsened model fields, while (d)-(f) use the diffusion/Markov-0 and Markov-1 models. Particles that fall within the mixed layer are not shown (see supporting information Text S2)

631 Figure 8 shows the particle distributions after 180 days of simulation, using advec-
 632 tion and the different subgrid-scale models on the coarsened flow data. Again, we repeat
 633 the domain in the zonal direction, so that we can distinguish particles that have crossed
 634 the periodic boundary. Figure 8c shows the obvious need for modeling subgrid-scale dis-
 635 persion when turbulent flow features are filtered out.

636 Figures 8d, e, and f show similar patterns when compared to one another, albeit
 637 with the dispersion in the LS case being somewhat weaker, and particles in the Markov-
 638 0 case reaching deeper than the others. Note that the diffusivity in the LS param-
 639 eterization is solely determined by derivatives of the flow fields. The pattern in 8e is qual-
 640 itatively similar to 8b, which bears testimony to the skill of the LS parameterization. Since
 641 the particles in the parameterizations each experience their own independent turbulent

642 fields, coherent structures and filamentation as seen in 8b cannot be reproduced by the
 643 Markov models.

644 In both Markov-0 models and in the Markov-1 model, we see some spurious partic-
 645 ple accumulation on the left side of the ridges (at $x = 500 \text{ km} + n * 1000 \text{ km}$, with
 646 $n = 0, 1, 2, \dots$). In the LS case, these accumulation patterns (or patterns where partic-
 647 les are fully absent) occur at other places too. In all cases this is likely due to sharp
 648 changes in the discrete derivatives used for computing the slopes that are necessary for
 649 filling the elements of \mathbf{K} , $\boldsymbol{\sigma}$, and $\boldsymbol{\theta}$. The LS parameterization relies on discrete deriva-
 650 tives of more quantities for computing its tensor elements, since these also depend on
 651 the shear of the flow (see (6)). It is therefore more susceptible to violations of the WMC
 652 when these discrete derivatives change strongly in space and interpolation is used.

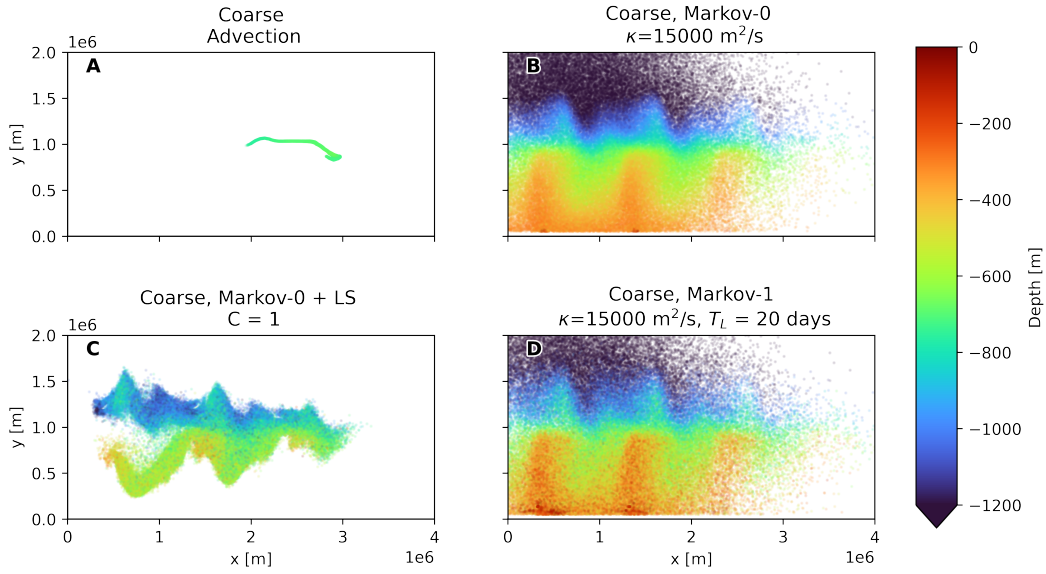


Figure 9. Like 8, with (a) advection in coarse-resolution model, (b)-(d) using the different subgrid-scale models.

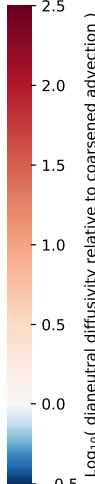
653 Figure 9 shows the spreading of Lagrangian particles in the coarse model. Again,
 654 the isotropic Markov-0 model and Markov-1 show a similar spread of particles, with par-
 655 ticles in Markov-0 again reaching slightly deeper depth. However, the LS parameteri-
 656 zation this time produces very different results, with the dispersion being much more lim-
 657 ited, and the particles being more concentrated. This means that in this case the shear-
 658 based parameterization leads to a much smaller diffusivities in \mathbf{K}_{LS} . This makes sense,
 659 as the fine-resolution flow field (and thus the coarsened flow) is full of baroclinic insta-
 660 bilities that lead to eddies with large shear. The resolution in the coarse model is too
 661 low for these instabilities to develop. Instead, the flow tends to a much smoother steady-
 662 state, with less shear. As this yields smoother derivatives in the temperature field (and
 663 in the velocity fields in the case of LS), this should lead to less spurious accumulation.
 664 Indeed we see no clear regions where particles accumulate.

665 4.6 Spurious dianeutral diffusivity

666 Two possible causes of spurious dianeutral tracer fluxes are numerical integration
 667 and interpolation of discrete, time-evolving Eulerian flow fields. The spurious dianeu-
 668 tral flux can be expressed as a diffusivity, and this diffusivity causes no complications

669 when it is smaller than the vertical diffusivity that is specified to represent dianeutral
 670 processes. For example, in the Southern Ocean, the average diapycnal diffusivity at 1500 m
 671 depth is estimated to be $1.3 \pm 0.2 \times 10^{-5} \text{ m}^2 \text{ s}^{-1}$ (Ledwell et al., 2011). It is important
 672 to assess how large the dianeutral diffusivities in our Lagrangian simulations become,
 673 and how they compare to the dianeutral diffusivity that we specify. In this section, we
 674 will assess these spurious dianeutral diffusivities. In these experiments, we specified an
 675 explicit dianeutral diffusivity of $1 \times 10^{-5} \text{ m}^2 \text{ s}^{-1}$. Moreover, in the case of the Markov
 676 models, we test several values of (effective) isoneutral diffusivities, keeping $T_L = 20$ days
 677 in the case of Markov-1. For Markov-0 combined with the LS parameterization, we choose
 678 different tuning parameters C at $\mathcal{O}(1)$, which affect the strength of the diffusivity.

Table 1. Effective dianeutral diffusivity (in $\text{m}^2 \text{ s}^{-1}$) for different depth classes with parameterizations applied on the *coarsened* flow field, after numerical integration for 180 days, with $\Delta t=40$ minutes. The color scale indicates the logarithm of the relative dianeutral diffusivity, when divided by the dianeutral diffusivity in the coarsened case per depth class as reference. This indicates the orders of magnitude that the dianeutral diffusivity differs from that in the simulations with only advection using coarsened fields. Of the parameterizations, Markov-1 has the lowest dianeutral diffusivity, in some cases even lower than in the simulation with advection only.

	All depths	$-200 \geq z > -600$	$-600 \geq z > -1200$	$-1200 \geq z \geq -1600$	
Fine advection	4.2E-04	1.1E-03	2.1E-04	1.9E-04	
Coarsened advection	3.8E-04	9.3E-04	1.9E-04	1.7E-04	
Markov-0, $\kappa=1500$	9.2E-04	1.4E-03	6.8E-04	9.0E-04	
Markov-0, $\kappa=5000$	3.1E-03	2.4E-03	2.4E-03	4.3E-03	
Markov-0, $\kappa=15000$	1.4E-02	5.2E-03	1.2E-02	1.8E-02	
Markov-0 + LS, $C=0.3$	8.6E-04	1.8E-03	5.8E-04	6.0E-04	
Markov-0 + LS, $C=1$	1.6E-03	2.6E-03	1.2E-03	1.5E-03	
Markov-0 + LS, $C=3$	5.0E-03	5.3E-03	3.9E-03	6.2E-03	
Markov-1, $\kappa=1500$	6.2E-04	1.3E-03	4.5E-04	4.0E-04	
Markov-1, $\kappa=5000$	5.6E-04	9.2E-04	5.6E-04	3.6E-04	
Markov-1, $\kappa=15000$	2.1E-04	3.7E-04	2.0E-04	1.5E-04	

679 We compute the effective dianeutral diffusivity in the case of pure advection using
 680 the fine-resolution, coarsened, and coarse-resolution fields, and using the Markov-
 681 0 and Markov-1 model. This dianeutral diffusivity is approximated as follows: for each
 682 particle, we record its initial local water density. Then, after simulating the particle's
 683 movement for 180 days, at the particle's new horizontal location, we compute the depth
 684 z_{iso} of the isopycnal corresponding to the original local water density. Comparing this
 685 depth with the particle's new depth, we can compute a spurious vertical diffusivity (sim-
 686 ilar to (25)). This again assumes that the dianeutral diffusivity is closely aligned with
 687 the vertical direction. We separate the results for three depth classes on which particles
 688 were released. Particle trajectories that at any point reach depths of -50 m or higher
 689 are excluded in these computations, in order to filter out effects related to particles en-
 690 tering the mixed layer (see supporting information Text S2).

691 The results are found in Table 1 for the coarsened flow and in Table 2 for the coarse-
 692 resolution flow. In all cases, the effective dianeutral diffusivities are higher than the value

Table 2. Same as Table 1, but using *coarse-resolution* flow fields. Again, Markov-1 has the lowest dianeutral diffusivity of the three parameterizations.

	All depths	-200 ≥ z > -600	-600 ≥ z > -1200	-1200 ≥ z ≥ -1600	
Coarse advection	2.6E-05	1.5E-05	2.4E-05	3.7E-05	
Markov-0, κ=1500	6.1E-04	1.8E-03	2.5E-04	1.9E-04	
Markov-0, κ=5000	1.8E-03	5.8E-03	7.4E-04	3.8E-04	
Markov-0, κ=15000	3.6E-03	7.7E-03	2.5E-03	2.6E-03	
Markov-0 + LS, C=0.3	3.6E-04	6.1E-04	2.4E-04	3.2E-04	
Markov-0 + LS, C=1	5.2E-04	8.4E-04	4.0E-04	4.2E-04	
Markov-0 + LS, C=3	1.1E-03	2.1E-03	8.8E-04	7.7E-04	
Markov-1, κ=1500	2.6E-04	5.7E-04	1.3E-04	1.9E-04	
Markov-1, κ=5000	3.2E-04	9.4E-04	1.1E-04	1.3E-04	
Markov-1, κ=15000	1.0E-04	3.9E-04	1.5E-05	2.0E-05	

693 of $1 \times 10^{-5} \text{ m}^2 \text{ s}^{-1}$ that we explicitly set, meaning that the spurious dianeutral diffusiv-
 694 ities due to errors in interpolation and the numerical schemes dominate. This is already
 695 the case for simulations that only use advection. We found that halving the timestep does
 696 not make a difference here, indicating that the error in the case of advection is likely not
 697 due to the time discretization. In the case of advection using fine-resolution data, the
 698 distance that a particle covers over the course of one flow snapshot, compared to the length
 699 of a grid cell, is relatively higher than in the case of coarse-resolution data, where it takes
 700 longer to traverse the larger cells. The dianeutral error can then be reduced by using more
 701 frequent snapshots of the data (e.g. 6-hourly snapshots instead of daily), such that tem-
 702 poral interpolation occurs over a smaller time window (Qin et al., 2014). This could how-
 703 ever come at a large expense in storage, memory and I/O. Here, we are solely interested
 704 in comparing the errors between different Lagrangian simulations, so we accept that the
 705 dianeutral diffusivities are higher than specified. In the coarsened and coarse-resolution
 706 fields, we use steady-state flows, meaning that the errors are due to spatial interpola-
 707 tion of coarse data, with time-interpolation playing no role.

708 Both Tables 1 and 2 show that for each experiment Markov-0 produces a much higher
 709 spurious dianeutral diffusivity than Markov-1. This corroborates the findings of section
 710 3.3. A likely explanation is that the isoneutral turbulent displacement in each of the mod-
 711 els becomes somewhat dianeutral as discrete neutral surfaces ‘curve’, but that the dis-
 712 placements in Markov-1 are much smaller than is the case for Markov-0. In the case of
 713 Markov-0, we see the error increasing as the diffusivity increases. This pattern cannot
 714 be seen for Markov-1, where in some cases, the error decreases with increasing effective
 715 diffusivity. Unfortunately, we do not have an explanation for this pattern.

716 Since the dianeutral diffusivity in the case of Markov-0 can become several orders
 717 of magnitude higher than is the case for only advection, future studies should be care-
 718 ful with applying this subgrid-scale dispersion parameterization. Here we implemented
 719 the Euler-Maruyama scheme. Higher-order schemes, such as the first order Milstein scheme,
 720 are able to greatly reduce the dianeutral error in idealized situations (Shah et al., 2011;
 721 Gräwe, 2011; Shah et al., 2013). However, we found that the Milstein-1 scheme produces
 722 similar dianeutral errors to Euler-Maruyama when applied on our coarsened and coarse-
 723 resolution flows, further indicating that the cause of the error lies in interpolation com-
 724 bined with large turbulent displacements.

5 Conclusion

We achieved two main goals with this study: formulating an isoneutral description of the Markov-1 model, and extending an anisotropic tracer diffusion parameterizations to the random walk dispersion/Markov-0 model. With these goals, we aim to improve the parameterization of unresolved isoneutral turbulent motions due to eddies in Lagrangian studies.

Because of the inclusion of a velocity autocorrelation, the Markov-1 model is able to produce both the ballistic and diffusive dispersion regime, and it produces particle trajectories and dispersion patterns that are more realistic than those produced by Markov-0. Our formulation of Markov-1, inspired by Redi's diffusion tensor, also has a much smaller spurious diapycnal flux than Markov-0, due to the smaller turbulent displacement in each timestep. Large turbulent displacements in the isoneutral direction in the presence of curvature in the neutral surfaces lead to diapycnal excursions. Therefore, our three-dimensional isoneutral formulation of Markov-1 will hopefully be useful to the Lagrangian community, with the many benefits of higher order stochastic models beyond Markov-1 given by previous studies (Griffa, 1996; Berloff & McWilliams, 2002; Veneziani et al., 2004). We also believe that the isoneutral formulation of the parameter tensors (16) and (17) is extendable to the parameter tensors of the higher order stochastic models beyond Markov-1, as well as other improvements to this model, like the inclusion of looping motions.

Further research into the isoneutral formulation of Markov-1, as well higher order stochastic models, may focus on better retaining the velocity autocorrelation on curved surfaces, which remains a complex issue (Gaspari & Cohn, 1999). Next to that, it may also further investigate boundary conditions further, as well as how Lagrangian particle models can transition from isoneutral dispersion in the ocean interior to horizontal and vertical mixing in the mixed layer, which has been left out of this study (see supporting information S2). Moreover, future studies employing isoneutral dispersion models may benefit from improved computation of neutral surface slopes (Groeskamp et al., 2019).

We hope that future Lagrangian studies using coarse fields, such as the output of coupled Earth system models, may also benefit from the LS parameterization, as well as other Eulerian anisotropic parameterizations based on closure. This may help automatically determine the strength of the eddy diffusivity in different regions in the domain. When applied to the coarsened flow field, the LS parameterization was able to produce particle distributions similar to the isotropic Markov models, meaning that LS may obviate the need for explicit parameter estimation in Markov-0. Our discussion of the LS parameterization may inspire further investigation into the application of closure schemes in Lagrangian simulations. Similarly, such closures could be further studied for the Markov-1 model, although so far Berloff and McWilliams (2003) tested a related closure based on shear with negative results.

Data and Software Availability Statement

Datasets (CC-BY) and analysis scripts (MIT license) for this research will become available with a DOI on YODA, Utrecht University's persistent research data management system. This includes MITgcm model generation scripts, data post-processing scripts, Parcels Lagrangian simulation scripts, and analysis scripts for generating figures and tables. For now, these can be accessed through the following open GitHub repository, as any revisions during the peer-review would change their content: <https://github.com/daanreijnders/isonneutral-dispersion>.

Acknowledgments

DR was supported through funding from the Netherlands Organization for Scientific Research (NWO), Earth and Life Sciences, through project OCENW.KLEIN.085. ED is an honorary research associate with the Belgian Fund for Scientific Research (F.R.S.-FNRS). EvS was supported through funding from the European Research Council (ERC) under the European Union’s Horizon 2020 research and innovation program (grant agreement 715386). We thank Syed Hyder Ali Muttaqi Shah for providing tips for numerically implementing SDE schemes. We also thank Pavel Berloff and Arnold Heemink for a useful discussion on the topic of this study.

References

- Abernathy, R., Busecke, J., Smith, T., Banihirwe, A., jldleauna, Bot, S., . . . Rath, W. (2021, May). *xgcm/xgcm: v0.5.2*. Zenodo. Retrieved from <https://doi.org/10.5281/zenodo.4821276> doi: 10.5281/zenodo.4821276
- Abernathy, R., Ferreira, D., & Klocker, A. (2013). Diagnostics of isopycnal mixing in a circumpolar channel. *Ocean Modelling*, *72*, 1–16. doi: 10.1016/j.ocemod.2013.07.004
- Abernathy, R., Marshall, J., & Ferreira, D. (2011). The Dependence of Southern Ocean Meridional Overturning on Wind Stress. *Journal of Physical Oceanography*, *41*(12), 2261–2278. doi: 10.1175/JPO-D-11-023.1
- Bachman, S. D., Fox-Kemper, B., & Bryan, F. O. (2020). A Diagnosis of Anisotropic Eddy Diffusion From a High-Resolution Global Ocean Model. *Journal of Advances in Modeling Earth Systems*, *12*(2). doi: 10.1029/2019MS001904
- Balwada, D., Smith, K. S., & Abernathy, R. (2018). Submesoscale Vertical Velocities Enhance Tracer Subduction in an Idealized Antarctic Circumpolar Current. *Geophysical Research Letters*, *45*(18), 9790–9802. doi: 10.1029/2018GL079244
- Berloff, P. S., & McWilliams, J. C. (2002). Material Transport in Oceanic Gyres. Part II: Hierarchy of Stochastic Models. *Journal of Physical Oceanography*, *32*, 34. doi: 10.1175/1520-0485(2002)032<0797:MTIOGP>2.0.CO;2
- Berloff, P. S., & McWilliams, J. C. (2003). Material Transport in Oceanic Gyres. Part III: Randomized Stochastic Models. *Journal of Physical Oceanography*, *33*, 30.
- Berloff, P. S., McWilliams, J. C., & Bracco, A. (2002). Material Transport in Oceanic Gyres. Part I: Phenomenology. *JOURNAL OF PHYSICAL OCEANOGRAPHY*, *32*, 33.
- Boussinesq, J. (1877). Essai sur la theorie des eaux courantes. *Memoires presentes par divers savants a l’Academie des Sciences de l’Institut National de France*, *23*(1).
- Campin, J.-M., Heimbach, P., Losch, M., Forget, G., edhill3, Adcroft, A., . . . raphael dussin (2020, July). *Mitgcm/mitgcm: mid 2020 version*. Zenodo. Retrieved from <https://doi.org/10.5281/zenodo.3967889> doi: 10.5281/zenodo.3967889
- Chelton, D. B., Deszoeke, R. A., Schlax, M. G., Naggar, K. E., & Siwertz, N. (1998). Geographical Variability of the First Baroclinic Rossby Radius of Deformation. *Journal of Physical Oceanography*, *28*, 28.
- Cox, M. D. (1987). Isopycnal diffusion in a z-coordinate model. *Ocean Modelling*.
- Danabasoglu, G., & McWilliams, J. C. (1995). Sensitivity of the Global Ocean Circulation to Parameterizations of Mesoscale Tracer Transports. *Journal of Climate*, *8*, 2967–297.
- Delandmeter, P., & van Sebille, E. (2019). The Parcels v2.0 Lagrangian framework: New field interpolation schemes. *Geoscientific Model Development*, *12*(8), 3571–3584. doi: 10.5194/gmd-12-3571-2019
- Fox-Kemper, B., Adcroft, A., Böning, C. W., Chassignet, E. P., Curchitser, E.,

- 825 Danabasoglu, G., ... Yeager, S. G. (2019). Challenges and Prospects
826 in Ocean Circulation Models. *Frontiers in Marine Science*, 6, 65. doi:
827 10.3389/fmars.2019.00065
- 828 Gaspari, G., & Cohn, S. E. (1999). Construction of correlation functions in two and
829 three dimensions. *Quarterly Journal of the Royal Meteorological Society*, 723–
830 757.
- 831 Gent, P. R., & McWilliams, J. C. (1990). Isopycnal Mixing in Ocean Circulation
832 Models. *Journal of Physical Oceanography*, 20(1), 150–155.
- 833 Gräwe, U. (2011). Implementation of high-order particle-tracking schemes in a water
834 column model. *Ocean Modelling*, 36(1), 80–89. doi: 10.1016/j.ocemod.2010.10
835 .002
- 836 Gräwe, U., Deleersnijder, E., Shah, S. H. A. M., & Heemink, A. W. (2012). Why the
837 Euler scheme in particle tracking is not enough: The shallow-sea pycnocline
838 test case. *Ocean Dynamics*, 62(4), 501–514. doi: 10.1007/s10236-012-0523-y
- 839 Griesel, A., Gille, S. T., Sprintall, J., McClean, J. L., LaCasce, J. H., & Maltrud,
840 M. E. (2010). Isopycnal diffusivities in the Antarctic Circumpolar Current
841 inferred from Lagrangian floats in an eddying model. *Journal of Geophysical
842 Research*, 115(C6), C06006. doi: 10.1029/2009JC005821
- 843 Griesel, A., McClean, J. L., Gille, S. T., Sprintall, J., & Eden, C. (2014). Eule-
844 rian and Lagrangian Isopycnal Eddy Diffusivities in the Southern Ocean of
845 an Eddying Model. *Journal of Physical Oceanography*, 44(2), 644–661. doi:
846 10.1175/JPO-D-13-039.1
- 847 Griffa, A. (1996). Applications of stochastic particle models to oceanographic prob-
848 lems. In R. J. Adler, P. Müller, & B. L. Rozovskii (Eds.), *Stochastic Modelling
849 in Physical Oceanography* (pp. 113–140). Boston, MA: Birkhäuser Boston. doi:
850 10.1007/978-1-4612-2430-3_5
- 851 Griffies, S. M. (1998). The Gent–McWilliams skew flux. *Journal of Physical
852 Oceanography*, 28(5), 831–841. doi: 10.1175/1520-0485(1998)0280831:TGMSF2
853 .0.CO;2
- 854 Groeskamp, S., Barker, P. M., McDougall, T. J., Abernathey, R. P., & Griffies,
855 S. M. (2019). VENM: An Algorithm to Accurately Calculate Neutral Slopes
856 and Gradients. *Journal of Advances in Modeling Earth Systems*, 11(7), 1917–
857 1939. doi: 10.1029/2019MS001613
- 858 Haigh, M., Sun, L., McWilliams, J. C., & Berloff, P. S. (2021). On eddy transport in
859 the ocean. Part II: The advection tensor. *Ocean Modelling*, 165, 101845. doi:
860 10.1016/j.ocemod.2021.101845
- 861 Haller, G., & Yuan, G. (2000). Lagrangian coherent structures and mixing in two-
862 dimensional turbulence. *Physica D: Nonlinear Phenomena*, 147(3-4), 352–370.
863 doi: 10.1016/S0167-2789(00)00142-1
- 864 Haza, A. C., Piterbarg, L. I., Martin, P., Özgökmen, T. M., & Griffa, A. (2007).
865 A Lagrangian subgridscale model for particle transport improvement and ap-
866 plication in the Adriatic Sea using the Navy Coastal Ocean Model. *Ocean
867 Modelling*, 17(1), 68–91. doi: 10.1016/j.ocemod.2006.10.004
- 868 Heemink, A. W. (1990). Stochastic modelling of dispersion in shallow water.
869 *Stochastic Hydrology and Hydraulics*, 4, 161–174.
- 870 Hewitt, H. T., Roberts, M., Mathiot, P., Biastoch, A., Blockley, E., Chassignet,
871 E. P., ... Zhang, Q. (2020). Resolving and Parameterising the Ocean
872 Mesoscale in Earth System Models. *Current Climate Change Reports*, 6(4),
873 137–152. doi: 10.1007/s40641-020-00164-w
- 874 Iacus, S. M. S. M. (2008). *Simulation and inference for stochastic differential equa-
875 tions: With R examples*. New York, N.Y.: Springer.
- 876 Klocker, A., Ferrari, R., & LaCasce, J. H. (2012). Estimating Suppression of Eddy
877 Mixing by Mean Flows. *Journal of Physical Oceanography*, 42(9), 1566–1576.
878 doi: 10.1175/JPO-D-11-0205.1
- 879 Klocker, A., Ferrari, R., Lacasce, J. H., & Merrifield, S. T. (2012). Reconciling float-

- 880 based and tracer-based estimates of lateral diffusivities. *Journal of Marine Re-*
 881 *search*, 70(4), 569–602. doi: 10.1357/002224012805262743
- 882 Kloeden, P. E., & Platen, E. (1999). *Numerical solution of stochastic differential*
 883 *equations* (No. 23). Berlin: Springer.
- 884 Koszalka, I., LaCasce, J. H., & Mauritzen, C. (2013). In pursuit of anom-
 885 alies—Analyzing the poleward transport of Atlantic Water with surface drifters.
 886 *Deep Sea Research Part II: Topical Studies in Oceanography*, 85, 96–108. doi:
 887 10.1016/j.dsr2.2012.07.035
- 888 LaCasce, J. H. (2008). Statistics from Lagrangian observations. *Progress in Oceanog-*
 889 *raphy*, 77(1), 1–29. doi: 10.1016/j.pocean.2008.02.002
- 890 Ledwell, J. R., St. Laurent, L. C., Girton, J. B., & Toole, J. M. (2011). Diapycnal
 891 Mixing in the Antarctic Circumpolar Current. *Journal of Physical Oceanogra-*
 892 *phy*, 41(1), 241–246. doi: 10.1175/2010JPO4557.1
- 893 Le Sommer, J., d’Ovidio, F., & Madec, G. (2011). Parameterization of subgrid
 894 stirring in eddy resolving ocean models. Part 1: Theory and diagnostics. *Ocean*
 895 *Modelling*, 39(1-2), 154–169. doi: 10.1016/j.ocemod.2011.03.007
- 896 Marshall, J., Adcroft, A., Hill, C., Perelman, L., & Heisey, C. (1997). A finite-
 897 volume, incompressible Navier Stokes model for studies of the ocean on parallel
 898 computers. *Journal of Geophysical Research: Oceans*, 102(C3), 5753–5766.
 899 doi: 10.1029/96JC02775
- 900 Marshall, J., & Speer, K. (2012). Closure of the meridional overturning circulation
 901 through Southern Ocean upwelling. *Nature Geoscience*, 5(3), 171–180. doi: 10
 902 .1038/ngeo1391
- 903 Mathieu, P.-P., & Deleersnijder, E. (1998). What is wrong with isopycnal diffusion
 904 in world ocean models? *Applied Mathematical Modelling*, 22(4), 367–378. doi:
 905 10.1016/S0307-904X(98)10008-2
- 906 McDougall, T. J. (1987). Neutral Surfaces. *Journal of Physical Oceanography*,
 907 17(11), 1950–1964. doi: 10.1175/1520-0485(1987)017<1950:NS>2.0.CO;2
- 908 McWilliams, J. C., Weiss, J. B., & Yavneh, I. (1994). Anisotropy and Coherent Vor-
 909 tex Structures in Planetary Turbulence. *Science*, 264(5157), 410–413. doi: 10
 910 .1126/science.264.5157.410
- 911 Nooteboom, P. D., Delandmeter, P., van Sebille, E., Bijl, P. K., Dijkstra, H. A., &
 912 von der Heydt, A. S. (2020). Resolution dependency of sinking Lagrangian
 913 particles in ocean general circulation models. *PLOS ONE*, 15(9), e0238650.
 914 doi: 10.1371/journal.pone.0238650
- 915 Nummelin, A., Busecke, J. J. M., Haine, T. W. N., & Abernathy, R. (2020).
 916 Diagnosing the Scale and Space Dependent Horizontal Eddy Diffusivity
 917 at the Global Surface Ocean. *Journal of Physical Oceanography*. doi:
 918 10.1175/JPO-D-19-0256.1
- 919 Piterbarg, L. I. (2002). The Top Lyapunov Exponent for a Stochastic Flow Modeling
 920 the Upper Ocean Turbulence. *SIAM Journal on Applied Mathematics*, 62(3),
 921 777–800. doi: 10.1137/S0036139999366401
- 922 Qin, X., van Sebille, E., & Sen Gupta, A. (2014). Quantification of errors induced by
 923 temporal resolution on Lagrangian particles in an eddy-resolving model. *Ocean*
 924 *Modelling*, 76, 20–30. doi: 10.1016/j.ocemod.2014.02.002
- 925 Redi, M. H. (1982). Oceanic Isopycnal Mixing by Coordinate Rotation. *Journal*
 926 *of Physical Oceanography*, 12(10), 1154–1158. doi: 10.1175/1520-0485(1982)
 927 012<1154:OIMBCR>2.0.CO;2
- 928 Reynolds, A. (2002). On Lagrangian stochastic modelling of material transport in
 929 oceanic gyres. *Physica D: Nonlinear Phenomena*, 172(1-4), 124–138. doi: 10
 930 .1016/S0167-2789(02)00660-7
- 931 Rodean, H. C. (1996). *Stochastic Lagrangian Models of Turbulent Diffusion*. Boston,
 932 MA: American Meteorological Society. doi: 10.1007/978-1-935704-11-9
- 933 Sallée, J. B., Speer, K., Morrow, R., & Lumpkin, R. (2008). An estimate of
 934 Lagrangian eddy statistics and diffusion in the mixed layer of the South-

- ern Ocean. *Journal of Marine Research*, 66(4), 441–463. doi: 10.1357/002224008787157458
- Sawford, B. L. (1991). Reynolds number effects in Lagrangian stochastic models of turbulent dispersion. *Physics of Fluids A: Fluid Dynamics*, 3(6), 1577–1586. doi: 10.1063/1.857937
- Shah, S. H. A. M., Heemink, A., & Deleersnijder, E. (2011). Assessing Lagrangian schemes for simulating diffusion on non-flat isopycnal surfaces. *Ocean Modelling*, 39(3-4), 351–361. doi: 10.1016/j.ocemod.2011.05.008
- Shah, S. H. A. M., Heemink, A. W., Gräwe, U., & Deleersnijder, E. (2013). Adaptive time stepping algorithm for Lagrangian transport models: Theory and idealised test cases. *Ocean Modelling*, 68, 9–21. doi: 10.1016/j.ocemod.2013.04.001
- Smagorinsky, J. (1963). General Circulation Experiments With the Primitive Equations: I. The Basic Experiment. *Monthly Weather Review*, 91(3), 99–164. doi: 10.1175/1520-0493(1963)0910099:GCEWTP2.3.CO;2
- Spagnol, S., Wolanski, E., Deleersnijder, E., Brinkman, R., McAllister, F., Cushman-Roisin, B., & Hanert, E. (2002). An error frequently made in the evaluation of advective transport in two-dimensional Lagrangian models of advection-diffusion in coral reef waters. *Marine Ecology Progress Series*, 235, 299–302. doi: 10.3354/meps235299
- Spivakovskaya, D., Heemink, A. W., & Deleersnijder, E. (2007). Lagrangian modelling of multi-dimensional advection-diffusion with space-varying diffusivities: Theory and idealized test cases. *Ocean Dynamics*, 57(3), 189–203. doi: 10.1007/s10236-007-0102-9
- Su, Z., Wang, J., Klein, P., Thompson, A. F., & Menemenlis, D. (2018). Ocean submesoscales as a key component of the global heat budget. *Nature Communications*, 9(1), 775. doi: 10.1038/s41467-018-02983-w
- Taylor, G. I. (1922). Diffusion by continuous movements. *Proceedings of the London Mathematical Society*, 2(1), 196–212.
- Thomson, D. J. (1987). Criteria for the selection of stochastic models of particle trajectories in turbulent flows. *Journal of Fluid Mechanics*, 180(-1), 529. doi: 10.1017/S0022112087001940
- van Sebille, E., Griffies, S. M., Abernathey, R., Adams, T. P., Berloff, P., Biastoch, A., ... Zika, J. D. (2018). Lagrangian ocean analysis: Fundamentals and practices. *Ocean Modelling*, 121, 49–75. doi: 10.1016/j.ocemod.2017.11.008
- van Sebille, E., Delandmeter, P., Lange, M., Kehl, C., Reijnders, D., Fischer, R., ... Vallès, I. (2020, October). *OceanParcels/parcels: Parcels v2.2.1: a Lagrangian Ocean Analysis tool for the petascale age*. Zenodo. Retrieved from <https://doi.org/10.5281/zenodo.4108148> doi: 10.5281/zenodo.4108148
- Veneziani, M., Griffa, A., Reynolds, A. M., Garraffo, Z. D., & Chassignet, E. P. (2005). Parameterizations of Lagrangian spin statistics and particle dispersion in the presence of coherent vortices. *Journal of Marine Research*, 63(6), 1057–1083. doi: 10.1357/002224005775247571
- Veneziani, M., Griffa, A., Reynolds, A. M., & Mariano, A. J. (2004). Oceanic Turbulence and Stochastic Models from Subsurface Lagrangian Data for the Northwest Atlantic Ocean. *Journal of Physical Oceanography*, 34, 23.
- Visser, A. (1997). Using random walk models to simulate the vertical distribution of particles in a turbulent water column. *Marine Ecology Progress Series*, 158, 275–281. doi: 10.3354/meps158275
- Wagner, P., Rühls, S., Schwarzkopf, F. U., Koszalka, I. M., & Biastoch, A. (2019). Can Lagrangian Tracking Simulate Tracer Spreading in a High-Resolution Ocean General Circulation Model? *Journal of Physical Oceanography*, 49(5), 1141–1157. doi: 10.1175/JPO-D-18-0152.1
- Wilson, J. D., & Flesch, T. K. (1993). Flow boundaries in random-flight dispersion models: Enforcing the well-mixed condition. *Journal of Applied Meteorology*

990 *and Climatology*, 32(11), 1695–1707. doi: 10.1175/1520-0450(1993)0321695:
991 FBIRFD2.0.CO;2
992 Wolfram, P. J., Ringler, T. D., Maltrud, M. E., Jacobsen, D. W., & Petersen, M. R.
993 (2015). Diagnosing Isopycnal Diffusivity in an Eddyding, Idealized Midlati-
994 tude Ocean Basin via Lagrangian, in Situ, Global, High-Performance Particle
995 Tracking (LIGHT). *Journal of Physical Oceanography*, 45(8), 2114–2133. doi:
996 10.1175/JPO-D-14-0260.1